

Evolution of U-Pb and Sm-Nd systems in numerical models of mantle convection and plate tectonics

Shunxing Xie¹

Department of Earth and Space Sciences, University of California, Los Angeles, California, USA

Paul J. Tackley

Department of Earth and Space Sciences and Institute of Geophysics and Planetary Physics, University of California, Los Angeles, California, USA

Received 15 May 2004; revised 13 August 2004; accepted 30 August 2004; published 18 November 2004.

[1] The development of U-Th-Pb and Sm-Nd isotopic signatures in a convecting mantle is studied using a numerical convection model with melting-induced differentiation and tracking of major and trace elements. The models include secular cooling and the decay of heat-producing elements, a rudimentary “self-consistent” treatment of plate tectonics, and both olivine system and garnet-pyroxene system phase transitions. The system self-consistently evolves regions with a high $\mu(=U/Pb)$ (HIMU)-like Pb signature and regions with low $^{143}Nd/^{144}Nd$. However, the isotopic “age” determined from the slope in $(^{207}Pb/^{204}Pb)-(^{206}Pb/^{204}Pb)$ space is much larger than observed. Several hypotheses are examined to explain this discrepancy. Sampling length scale has a minimal effect on age. The extent of crustal settling above the core-mantle boundary makes some difference but not enough. More frequent remelting is a possible explanation but requires the rate of crustal production to have been much higher in the past. Not introducing HIMU into the mantle prior to 2.0–2.5 Gyr before present, because of a change in the surface oxidization environment or subduction zone processes, can account for the difference, but its effect on other isotope systems needs to be evaluated. Improved treatment of the stretching of heterogeneities, which reduces them to length scales at which they cease to be identifiable magma sources, greatly reduces the Pb-Pb age. The mantle develops substantial chemical stratification from a homogeneous start, including stratification around 660 km caused by the two-component phase transitions. A deep layer of subducted crust may provide storage for some of the “missing” heat-producing elements. Magmatic heat transport is important in the first 2 Gyr of model time. *INDEX*

TERMS: 1010 Geochemistry: Chemical evolution; 1025 Geochemistry: Composition of the mantle; 1040 Geochemistry: Isotopic composition/chemistry; 8120 Tectonophysics: Dynamics of lithosphere and mantle—general; 8124 Tectonophysics: Earth’s interior—composition and state (1212); *KEYWORDS:* thermochemical convection, phase transitions, geochemical heterogeneity, isotopic age, mantle melting, isotopic fractionation

Citation: Xie, S., and P. J. Tackley (2004), Evolution of U-Pb and Sm-Nd systems in numerical models of mantle convection and plate tectonics, *J. Geophys. Res.*, 109, B11204, doi:10.1029/2004JB003176.

1. Introduction

1.1. Geochemical Constraints

[2] The observed geochemical signature of erupted magmas gives information about mantle material because mantle convection transports deep material into the shallow region where melting occurs [Hofmann, 1997]. Isotopic observations suggest that mid-ocean ridge basalt (MORB) is uniformly depleted in incompatible elements, while oceanic island basalt (OIB) is enriched and has a composi-

tion that varies from one region to another, or even in the same region.

[3] Chemical heterogeneity is observed at all scales [Carlson, 1987, 1994; Meibom and Anderson, 2004], even within the relatively uniform MORB source. For example, at the smallest scale (i.e., melt inclusions), Pb isotope ratios in OIB span a large fraction of the global range [Saal et al., 1998], while Nd ratios in the Ronda peridotite massif in Spain exceed the global OIB Nd ratio variation [Reisberg and Zindler, 1986]. Indeed, mantle rocks have been observed to contain some proportion of centimeter to meter scale veins of pyroxene-rich lithologies [Suen and Frey, 1987; Pearson et al., 1993]. Such variations have been used to suggest a “marble cake” style of chemical variation in the mantle, where small volumes of enriched material reside within a matrix of

¹Also at ReachLocal, Inc., Encino, California, USA.

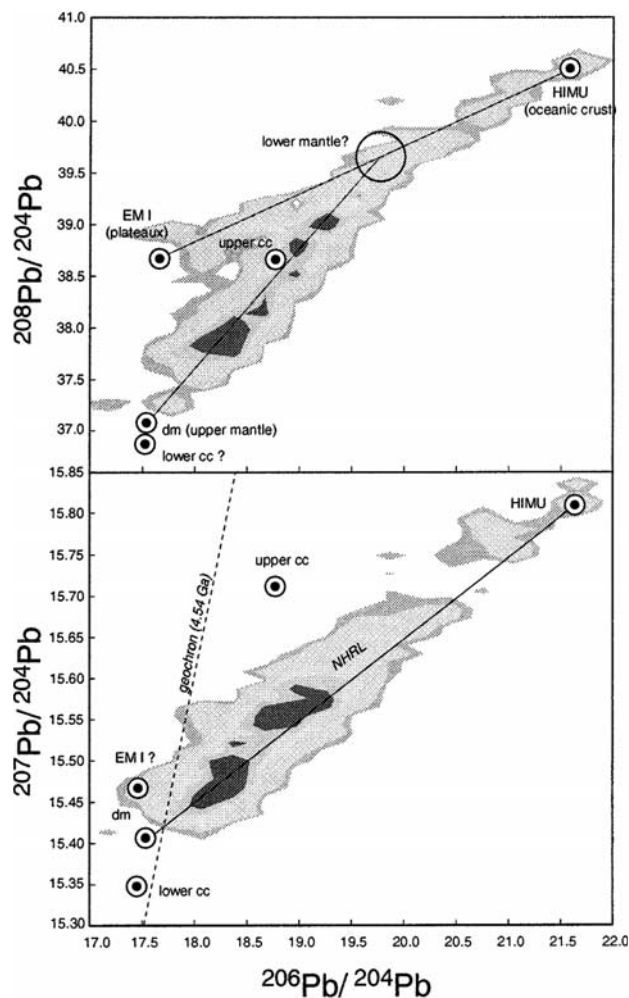


Figure 1. Observed data spread in (top) the $^{208}\text{Pb}/^{204}\text{Pb}$ versus $^{206}\text{Pb}/^{204}\text{Pb}$ diagram and (bottom) the $^{207}\text{Pb}/^{204}\text{Pb}$ versus $^{206}\text{Pb}/^{204}\text{Pb}$ diagram. (Reprinted from Albarède [2001], copyright 2001, with permission from Elsevier.)

depleted MORB mantle [Allègre and Turcotte, 1986], or a multicomponent, multiple-length-scale mixture of different “plums” with no uniform matrix [Meibom and Anderson, 2004; Morgan and Morgan, 1999]. There is also abundant evidence for compositional heterogeneity at scales of >1000 km [Schilling, 1973; Klein et al., 1988; Dupré and Allègre, 1983; Hart, 1984].

[4] The isotopic signature of OIBs is commonly interpreted to be the result of mixing four or more components in the mantle [Zindler and Hart, 1986], with the four components being depleted MORB mantle (DMM), high μ (=U/Pb) (HIMU), and enriched mantle types I and II (EMI and EMII, respectively). According to Carlson [1994], HIMU, EMI, and EMII may represent basaltic oceanic crust, continental lithospheric mantle or pelagic sediment, and terrigenous sediment, respectively.

[5] Isotope ratios evolve along separate paths in different materials due to fractionation of radiogenic parent and daughter elements during melting and subsequent radiogenic ingrowth of daughter isotopes. The resulting slopes on isotope diagrams indicates an age of fractionation and are widely used to date geological processes.

[6] In this paper we focus on Pb-Pb and Sm-Nd systems (i.e., the ratios $^{206}\text{Pb}/^{204}\text{Pb}$, $^{207}\text{Pb}/^{204}\text{Pb}$, $^{208}\text{Pb}/^{204}\text{Pb}$, and $^{143}\text{Nd}/^{144}\text{Nd}$), as the other isotope systems correlate with these in the simple treatment considered here. The observed ratio distributions are plotted in Figures 1 and 2. The highly radiogenic high Pb ($^{206}\text{Pb}/^{204}\text{Pb}$ end-member), as found in some OIB (e.g., the St. Helena Island basalts) is known as HIMU because it must have high U/Pb. Plots of $^{207}\text{Pb}/^{204}\text{Pb}$ – $^{206}\text{Pb}/^{204}\text{Pb}$ display a coherent line, from which an “effective age” can be calculated. The Pb-Pb isochron ages for various MORB and OIB groups correspond to effective ages of 1.5 to 2 Gyr [Hofmann, 1997], although the exact meaning of these ages is unclear. Sm-Nd plots do not display a clear line because of Sm/Nd fractionation during melting. The U-Pb system does not suffer this problem since the U/Pb ratio is not involved in the age calculation. MORB and most OIBs have $^{143}\text{Nd}/^{144}\text{Nd}$ greater than bulk Earth, and thus positive ϵ_{Nd} , where ϵ_{Nd} is the relative deviation of the $^{143}\text{Nd}/^{144}\text{Nd}$ ratio from the chondritic ratio (presently 0.512638) in parts per 10^4 . The spread of ϵ_{Nd} is much smaller in Archean-derived rocks which may then indicate faster mantle convection [Blichert-Toft and Albarède, 1994].

[7] Another constraint from these diagrams is that all oceanic basalts and most MORB plot to the high $^{206}\text{Pb}/^{204}\text{Pb}$ side of the geochron, implying that the mantle has experienced a net increase in μ (U/Pb). White [1993] found that the ratio μ in the depleted mantle is around 6, while the time-integrated value of the mantle is between 8 or 9, suggesting the presence of a reservoir with high μ .

1.2. Generation of End-Members by Recycling

[8] The HIMU end-member is commonly identified as subducted oceanic crust [Chase, 1981; Allègre and Turcotte, 1986; Christensen and Hofmann, 1994], which is enriched in incompatible trace elements because they preferentially partition into the melt during pressure-release melting underneath spreading centers, leaving behind a depleted residue. While this fractionates Nd and Sm because of their different partition coefficients, the generation of high U/Pb (HIMU) in oceanic crust is probably due to other processes, particularly hydrothermal removal of Pb from the subducted slab into subduction-related magmas [Hofmann, 1988] and enrichment of the oceanic crust in continental U carried by eroded sediments. Subducted slabs carry this HIMU crust and the depleted residue into the deep mantle. The differing Pb-Pb isochron age of different island chains (between 1 and 2.5 Gyr) was interpreted by Chase [1981] to correspond to the time of formation of the piece of oceanic crust that is being sampled. This process generates three distinct components: the original material, subducted crust, and depleted residue. Other components such as EMI and EMII probably involve continental material and are not included in the present study.

[9] What happens to these components after subduction depends on the dynamics of the system. If slabs reach the core-mantle boundary (CMB) and the crustal component is denser than its surroundings, then a significant fraction of the crust can settle into a layer above the CMB [Christensen

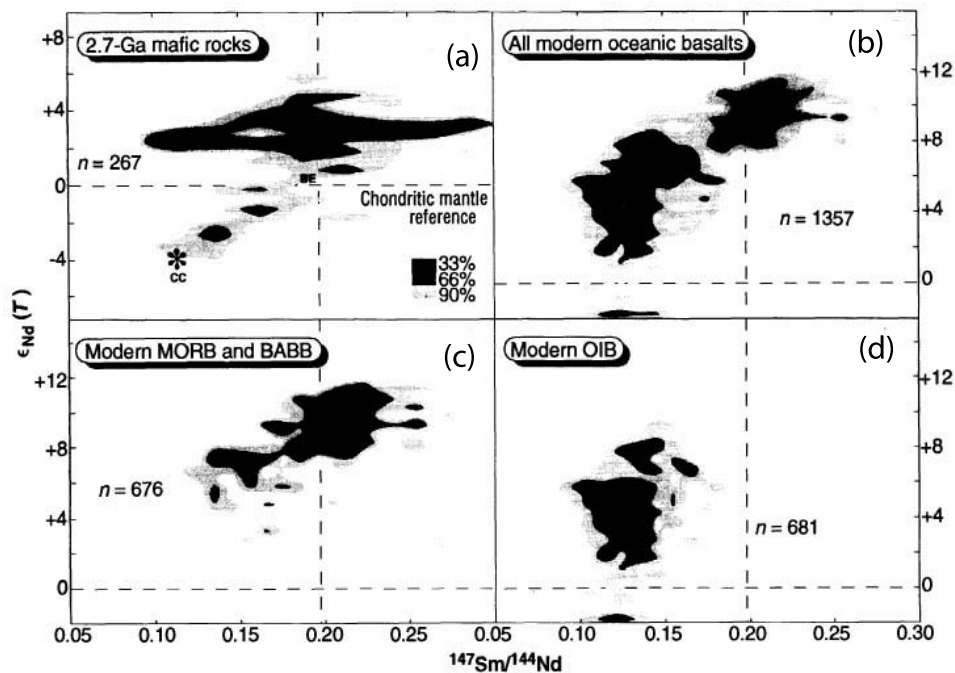


Figure 2. Isotopic composition of Nd as a function of Sm/Nd ratio among (a) late Archean mantle derived rocks, (b) modern oceanic basalts which include ocean island basalt (OIB), mid-ocean ridge basalt (MORB), and back-arc basin basalt (BARB), (c) modern MORB and BARB, and (d) modern OIB. (Reprinted with permission from *Blichert-Toft and Albarède* [1994]. Copyright 1994 AAAS.)

and Hofmann, 1994], from which plumes that generate OIB have been suggested to arise. However, the density contrast of crustal materials in the deepest mantle is uncertain. Ringwood [1990] proposed that basalt remains 2–4% denser than peridotite throughout the whole mantle, with the exception of the depth range 660–720 km, where it is less dense and might become trapped. However, Ono *et al.* [2001] estimated that the density profile of MORB intersects an average mantle density at around 1500–2000 km depth in the lower mantle, making MORB neutrally buoyant at a depth around 1600 km and positively buoyant at greater depths. In summary, the CMB region and 660–720 km depth may be possible locations for a crustal-enriched layer. Long-term storage of subducted oceanic crust may be necessary to explain geochemical signatures; for example the positive ϵ_{Nd} anomaly of Archean rocks [Chase and Patchett, 1988].

[10] Material that does not segregate into a layer is subject to mantle stirring and mixing processes, which have been estimated to mix the mantle rather quickly. For example, Hoffman and McKenzie [1985] concluded that subducted lithosphere would be mixed in less than half a billion years. While Gurnis and Davies [1986a] appeared to offer a solution by showing that with simple, weakly time-dependent kinematic flows and passive tracers, high deep-mantle viscosity could allow regions of chemical heterogeneity to survive for up to ~ 2 Gyr, subsequent calculations with more realistic time-dependent flows once again indicated a mixing time of several hundred million years either for whole mantle convection or two-layer convection [Christensen, 1989; Kellogg and Turcotte,

1990]. This rapid stirring is associated with the chaotic mixing regime, in which the accumulated strain or the thickness of heterogeneity varies exponentially with time. With such flows, high deep-mantle viscosity has only a small effect on mixing times [Van Keken and Ballentine, 1998, 1999; Ferrachat and Ricard, 2001].

[11] It appears difficult to reconcile these model mixing times with the ~ 1.5 –2 Gyr effective age of the DMM-HIMU trend, which has led some geochemists to propose that mantle convection is layered at the 660 km discontinuity, with a well-mixed upper mantle and a primitive lower mantle. However, such layering is in direct contradiction of a number of geophysical observations, particularly recent high-resolution seismic tomography models that clearly show slab penetration into the deepest mantle [Masters *et al.*, 2000; van Der Hilst *et al.*, 1997]. Instead, a thin layer (D'') above the CMB, related to seismologically observed heterogeneous structures in that region, has been widely proposed in the geophysical community, and is a possible source of enriched signatures in ocean island basalts [Hofmann and White, 1982]. The origin of the D'' seismic discontinuity may also be related to a postperovskite phase transition [Oganov and Ono, 2004; Murakami *et al.*, 2004].

1.3. Numerical Modeling

[12] Christensen and Hofmann [1994] studied the evolution of the common isotopic systems such as U-Pb in a numerical mantle convection model that included tracking of geochemical major and trace element species and an imposed time-dependent plate-like upper boundary con-

dition. In their calculations, a fraction of subducted crust segregated into a layer above the CMB, and for some parameter combinations they obtained realistic Pb-Pb isotope diagrams and “ages.” However, they found it necessary to run the calculations for only 3.6 Gyr, instead of the full age of the Earth; otherwise, the age was too high, contrary to previous expectations that it would be difficult to obtain a large enough age. Furthermore, their model mantle had a constant convective vigor (e.g., velocities, rate of melting), rather than, as is commonly believed, having a vigor that decreases with time as the mantle temperature and radiogenic heat production decrease.

[13] *Davies* [2002] also presented models of mantle convection in which subducted crust was tracked. The models were entirely heated from within, and although they had a constant convective vigor, greater vigor in the past was accounted for by a parameterized scaling between Earth time and model time. Although isotope diagrams were not calculated, he also found that the obtained mean ages (i.e., time since melting) are substantially larger than the observed isotopic ages. Clearly, obtaining large enough ages is not a problem in convection calculations with tracer-based compositional treatments; instead the problem is that the obtained ages are too large.

[14] In this paper, these issues are investigated by modeling mantle thermochemical evolution using a numerical convection model that combines a treatment of major and trace element geochemical evolution with a dynamically consistent mantle convection-plate tectonics model, essentially following on from *Christensen and Hofmann* [1994]. It is found, however, that the more “realistic” physical model employed here results in important modifications to their conclusions. The most important differences to their model are a convective vigor that decreases with time due to secular cooling and the decay of heat-producing elements, and the investigation of 4.5 Gyr run times as well as 3.6 Gyr. These differences result in a lot of differentiation early in the modeled evolution, which results in Pb-Pb ages that are much too large. Several hypotheses for the discrepancy are investigated. Noble gas evolution in a convecting mantle is studied by *Xie and Tackley* [2004].

2. Numerical Model and Methods

2.1. Physical Model

[15] A two-dimensional (2-D) cylindrical geometry is assumed [*Tackley and Xie*, 2002, 2003] with the core size scaled to give the same ratio of CMB surface area to outer surface area as in spherical geometry [*Van Keken*, 2001]. The infinite Prandtl number and compressible anelastic approximations are made [*Tackley*, 1996a]. The equations, nondimensionalized to the mantle depth (D), thermal diffusion timescale (D^2/κ , where κ is thermal diffusivity) and superadiabatic drop, ΔT_{sa} , are those of

Continuity

$$\nabla \cdot (\bar{\rho}\mathbf{v}) = 0 \quad (1)$$

Conservation of momentum

$$\nabla \cdot \left[\eta \left(\mathbf{v}_{ij} + \mathbf{v}_{j,i} - \frac{2}{3} v_{k,k} \delta_{ij} \right) \right] - \nabla p = Ra \hat{\mathbf{z}} \rho(C, z, T) / \Delta \rho_{\text{thermal}} \quad (2)$$

Conservation of energy

$$\begin{aligned} \bar{\rho} \bar{C}_p \frac{DT}{Dt} = & -Di_s \bar{\alpha} \bar{\rho} T v_z + \nabla \cdot (\bar{k} \nabla T) + \bar{\rho} H \\ & + \frac{Di_s}{Ra} \eta \left(\mathbf{v}_{ij} + \mathbf{v}_{j,i} - \frac{2}{3} v_{k,k} \delta_{ij} \right) v_{i,j} \\ & + \bar{C}_p \frac{Di_s T}{\bar{\rho}} \sum_{i=1}^{n_{\text{phase}}} f_i P_i \frac{d\Gamma_i}{dz} v_z \end{aligned} \quad (3)$$

Conservation of bulk chemistry

$$\frac{\partial C}{\partial t} + \mathbf{v} \cdot \nabla C = 0 \quad (4)$$

where the surface dissipation number Di_s is given by

$$Di_s = \frac{\alpha_s g D}{C_p s} \quad (5)$$

and reference Rayleigh number Ra is given by

$$Ra = \frac{\rho_s g \alpha_s \Delta T_{sa} D^3}{\eta(T_{as}, 0) \kappa_s} \quad (6)$$

The variables are temperature T , composition C , velocity \mathbf{v} , and pressure p . The governing parameters are Rayleigh number Ra , internal heating rate H , and surface dissipation number Di_s . Material properties with overbars (density $\bar{\rho}$, thermal expansivity $\bar{\alpha}$, and thermal conductivity \bar{k}) vary with depth only, specific heat capacity C_p is constant, $\Delta \rho_{\text{thermal}}$ is the fractional density variation with temperature ($\alpha_{\text{dimensional}} \Delta T_{\text{dimensional}}$) and $\rho(C, z, T)$ is discussed in equation (14); $\hat{\mathbf{z}}$ is a unit vector in the vertical direction, g is the gravitational acceleration and T_{as} is the surface temperature of the reference adiabat. Chemical diffusion is neglected, which corresponds to an infinite Lewis number $Le = \kappa/C_f$, where C_f is the chemical diffusivity. P_i is the usual phase buoyancy parameter for the i th phase change [*Christensen and Yuen*, 1985; *Tackley et al.*, 1994], f_i is the fraction of the relevant component in the assemblage and Γ_i is (depth-dependent) phase function. f_i and Γ_i are detailed in section 2.3.2. Numerically, adiabatic effects resulting from vertical motion (heating/cooling and latent heat) are dealt with by advecting potential temperature, rather than by coding the terms in equation (3), as this avoids problems that might result from steep gradients in, for example, Γ_i .

[16] Table 1 lists assumed parameters. H is not listed because it depends on the concentration of heat producing elements, which varies with position and time, and is thus calculated for each time step and grid cell as discussed in section 2.3.6. A thermodynamic model is used to calculate the depth variation of material properties density $\bar{\rho}$, thermal expansivity $\bar{\alpha}$, and thermal conductivity \bar{k} , as detailed in previous papers [*Tackley*, 1996a, 1998; *Tackley and Xie*, 2003].

Table 1. Thermodynamic Parameters

Parameter	Symbol	Value	Units	Non-D Value
<i>Input Nondimensional Parameters</i>				
Reference Ra	Ra_s	-	-	1.3×10^7
Surface dissipation	Di_s	-	-	1.18
Mean dissipation	$\langle Di_s \rangle$	-	-	0.38
Surface Gruneisen	γ_s	-	-	1.1
<i>Nominal Dimensional Parameters</i>				
Depth of mantle	D	2890	km	1.0
Superadiabatic temperature drop	ΔT_{sa}	2500	K	1.0
Temperature, surface	T_s	300	K	0.12
Expansivity, surface	α_s	5.0×10^{-5}	K^{-1}	1.0
Conductivity, surface	k_s	3.0	$W m^{-1} K^{-1}$	1.0
Heat capacity	C_p	1200	$J kg^{-1} K^{-1}$	1.0
Density, surface	ρ_s	3300	$Kg m^{-3}$	1.0
Reference viscosity	η_{ref}	1.0	$10^{22} Pa.s$	1.0
Yield stress	σ_{yield}	100	MPa	1.1×10^5
Latent heat	L	600	$kJ kg^{-1}$	0.2

[17] Viscosity η depends on temperature and vertical coordinate z :

$$\eta(T, z) = \eta_0 e^{-(T-T_{0\eta})E_\eta + (z-z_{0\eta})V_\eta} [1 + 9H(0.7716 - z)] \quad (7)$$

where E_η is 13.8155, giving a factor of 10^6 viscosity change for a temperature change of nondimensional 1.0, and V_η is 4.6, which gives a hundredfold increase in viscosity between the surface and CMB along an isotherm (less than that along an adiabat). Additionally the last term gives a factor of 10 increase in viscosity at 660 km depth (H is the Heaviside step function); η_0 is set such that $\eta(T_{0\eta}, z_{0\eta}) = 1.0$, where $T_{0\eta} = 0.64$ (dimensional 1600 K) and $z_{0\eta} = 0$. Such strong temperature dependence gives rigid lid convection [e.g., *Moresi and Solomatov*, 1995; *Solomatov and Moresi*, 1996], so in order to break the lid a yield stress is introduced, which represents ductile, semibrittle processes and leads to a rudimentary form of plate-like behavior [*Moresi and Solomatov*, 1998; *Tackley*, 2000a, 2000b]. The yield stress is assumed to be 100 MPa at the surface, increasing linearly by a factor of 5 to the CMB. This yielding is implemented using an effective viscosity, defined as

$$\eta_{eff} = \min \left[\eta(T, z), \frac{\sigma_{yield}}{2\dot{\epsilon}} \right] \quad (8)$$

where $\dot{\epsilon}$ is the second invariant of the deviator strain rate tensor:

$$\dot{\epsilon} = \sqrt{\frac{1}{2} \epsilon_{ij} \dot{\epsilon}_{ij}} \quad (9)$$

The equations are solved using the finite volume multigrid code STAG3D, as extensively used previously [e.g., *Tackley*, 1996a, 2000a, 2000b], with 256 evenly spaced cells in the azimuthal direction and 64 unevenly spaced cells (giving refinement in the boundary layers) in

the radial direction. Compositional variations are tracked using tracer particles, as detailed by *Tackley* [2002b] and *Tackley and King* [2003], with the addition that each tracer carries a certain mass (number of atoms) of each trace element. Compressibility does not require any special tracer treatment, because when moving to regions of higher or lower density, tracers will automatically get closer together or further apart (due to convergence or divergence of the velocity field) by the amount needed to maintain a uniform tracer density per mass of mantle, hence concentration of trace elements. Approximately 400,000 tracers are used, averaging 25 per grid cell.

2.2. Boundary Conditions and Core Cooling

[18] Top and bottom boundaries are impermeable, free-slip, and isothermal, while side boundaries are periodic. Cooling of the core due to heat conducted into the mantle is accounted for using a simple model in which the CMB temperature decreases as heat is removed. *Van Keken* [2001] showed that the CMB heat flux in a cylindrical model with rescaled core radius is essentially the same as that in a spherical model with the normal core radius; thus we here assume a spherical core with the correct radius for calculating core cooling. The core is assumed to be always in internal thermodynamic equilibrium (i.e., has infinite effective thermal conductivity) and homogeneous (i.e., using mean parameters for inner and outer core). The dimensional equation solved for the core's parameterized cooling is [*Steinbach and Yuen*, 1994]:

$$r_c \rho_c C_c \frac{dT_c}{dt} = -3q_c \quad (10)$$

where ρ_c denotes mean core density (approximately $11,000 kg m^{-3}$), C_c specific heat (approximately $5 \times 10^2 J kg^{-1} K^{-1}$), T_c temperature and q_c heat flux from the core, and r_c core radius ($3.485 \times 10^6 m$).

[19] After nondimensionalizing equation (10) to the standard scales given in Table 1, the following form is obtained:

$$dT_n = -\frac{3q_n}{r_n \rho_n C_n} dt_n \quad (11)$$

Table 2. Phase Transition Properties^a

	Depth, km	T , K	$\Delta\rho$, kg m ⁻³	γ , MPa K ⁻¹
<i>Olivine System</i>				
1	410	1600	280	+2.5
2	660	1900	400	-2.5
<i>Pyroxene-Garnet System</i>				
1	60	0	350	0
2	400	1600	150	+1.0
3	720	1900	500	+1.0

^aThe parameter γ is the Clapeyron slope.

where the subscript n denotes nondimensionalized value. Using $r_n = 1.2059$, $\rho_n = 3.3$, and $C_n = 0.42$ yields

$$dT_n = -\frac{q_n}{0.5575} dt_n \quad (12)$$

2.3. Chemical Model

2.3.1. Major Elements and Melting

[20] Both major and trace elements are tracked in the model, which is designed to represent the mantle-oceanic plate system, i.e., continents are not present. For major elements, a two-component system is assumed, the end-members being crust/eclogite and harzburgite. The variable C , which varies from 0 to 1, represents the fraction of crustal material present, and is initialized at $C = 0.3$ everywhere. Oceanic crust is formed self-consistently by melting and differentiation, which occurs as a separate substep to solving equations (1)–(4), as in previous studies [Tackley and Stevenson, 1993; Scott and Stevenson, 1989], as follows. After time-stepping equation (3), the temperature in some cells may exceed the solidus, which is here based on a fit to experimental data [Zerr *et al.*, 1998; Herzberg *et al.*, 2000] and is composition-independent, except that no melting can occur once the basaltic component has been completely removed (i.e., $C = 0$). The melting substep occurs in these supersolidus cells and involves generating, where sufficient basalt fraction exists, the fraction of partial melt f that brings the temperature back to the solidus, i.e.,

$$f = \min[(T - T_{\text{sol}}(z))/L, C] \quad (13)$$

and $T \rightarrow T - Lf$, where L is the latent heat. The melt is then instantly removed and deposited at the surface to form crust. With this approach, residue from melting is depleted only by the amount needed to generate the formed crust; it is not necessarily $C = 0$ harzburgite. Chemical density variation depends on depth and composition with both olivine and garnet-pyroxene phase changes implemented, as discussed in section 2.3.2.

2.3.2. Multiple Phase Transitions

[21] A simple parameterization is implemented based on mineral physics data [e.g., Ringwood, 1990; Ono *et al.*, 2001]. Minerals are divided into the olivine system and the pyroxene-garnet (px-gt) system, which undergo different phase transitions (Table 2). Thus the mixture of minerals depends on composition, pressure (due to solid-solid phase transitions), and temperature (due to their finite Clapeyron slopes). The chemical composition C is mapped linearly

into the fraction of the different phase systems, with $C = 1$ (basalt) corresponding to pure px-gt and $C = 0$ (harzburgite) corresponding to 6/7 olivine and 1/7 px-gt. Thus the olivine fraction $f_{\text{ol}} = \frac{6}{7}(1 - C)$. For calculating mean density it is assumed that the systems can be added linearly, leading to [Tackley and Xie, 2003]

$$\rho(f_{\text{ol}}, z, T) = [f_{\text{ol}}\bar{\rho}_{\text{ol}}(z, \bar{T}) + (1 - f_{\text{ol}})\bar{\rho}_{\text{px-gt}}(z, \bar{T})] \times [1 - \alpha_{\text{eff}}(T - \bar{T}(z))\Delta\rho_{\text{thermal}}] \quad (14)$$

where the $\bar{\rho}(z, T)$ terms depend on depth and the last term accounts for thermal expansion and phase change buoyancy. $\bar{T}(z)$ is the reference adiabat (1600 K potential temperature). The calculation of the reference state density profile is fully detailed by Tackley [1996a], the only extension being the addition of density jumps at the phase transition depths [Tackley, 1998].

[22] The effective thermal expansivity due to phase transitions is an extension of that used in previous studies [Christensen and Yuen, 1985] and is given by

$$\alpha_{\text{eff}} = \bar{\alpha}(z) + \sum_{i=1}^{n\text{phase}} f_i P_i \frac{d\Gamma_i}{dz} \quad (15)$$

where for the i th phase change, P_i is the phase buoyancy parameter, f_i is the fraction of the relevant component in the assemblage (f_{ol} for olivine phase transitions and $(1 - f_{\text{ol}})$ for pyroxene-garnet phase transitions) and Γ_i is the phase function, which varies from 0 above a phase transition to 1 below it. Here, the “sheet mass anomaly” approximation is used [Tackley *et al.*, 1994; Tackley, 1996b], which is equivalent to Γ changing from 0 to 1 linearly across one fixed vertical grid level, such that the mass anomalies are concentrated into that grid level.

[23] The density profile of the px-gt component is not well constrained through the lower mantle, with some authors suggesting that it may become less dense than the pyrolite composition at high pressure [e.g., Ono *et al.*, 2001]. Thus three different compressibilities are considered for the px-gt system in the lower mantle, leading to it being either more dense, equally dense or less dense at the CMB than the olivine system. This leads to the density profiles shown in Figure 3. Note that the shallow (60 km depth) transition in the pyroxene-garnet system leads to the basalt-eclogite transition.

2.3.3. Trace Elements

[24] The trace element isotopes ²³⁵U, ²³⁸U, ²³²Th, ⁴⁰K, ²⁰⁴Pb, ²⁰⁶Pb, ²⁰⁷Pb, ¹⁴³Nd, ¹⁴⁴Nd, and ¹⁴⁷Sm, are included. These are tracked using tracer particles; each tracer carries a certain amount (mass) of each trace element isotope (Table 3). Sections 2.3.4–2.3.7 give details of their initial concentrations, fractionation on melting, radiogenic decay, and age determination.

2.3.4. Initial Concentrations

[25] As the model does not include continental crust forming processes, it is assumed, following Christensen and Hofmann [1994], that the continental crust has already been extracted. Current bulk mantle concentrations of the various isotopes are listed in Table 3. It is estimated that the present abundance of U in primitive mantle is about

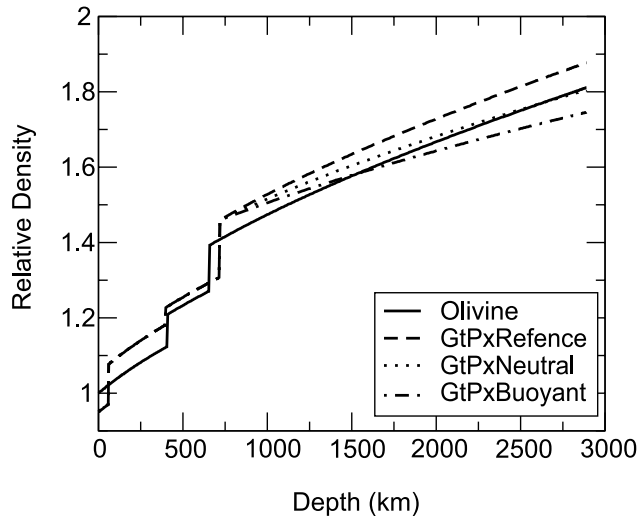


Figure 3. Density variation along a reference adiabat for the two phase systems. GtPxReference, GtPxNeutral, and GtPxBuoyant are the density profiles with px-gt being more dense, equally dense, or less dense at the CMB than the olivine system, respectively.

2.6 times the value in CI chondrites, or double the value in ordinary chondrites [Jochum *et al.*, 1983]. If a value of $U = 0.008$ ppm is used for CI chondrite, a primitive mantle abundance of $U = 21$ ppb is obtained. The study here uses $U = 18.5$ ppb, to account for the extraction of the continental crust. The Th/U ratio of the bulk Earth is known from Pb isotopes systematics to be about 3.8 [Doe and Zartman, 1979]. A value of $K/U = 1.27 \times 10^4$ has been measured for the MORB source mantle and can be applied to the bulk Earth [Jochum *et al.*, 1983].

[26] Initial concentrations are determined from present-day concentrations using the standard radioactive decay equations, which are usually written in terms of isotope ratios rather than absolute abundances. Present-day mean mantle isotope ratios are taken from [Christensen and Hofmann, 1994; Hofmann, 1997]. As ^{147}Sm decay produces an insignificant amount of heat and only isotope ratios are used, the absolute concentration of Nd and Sm has no effect on the results; the concentration of ^{144}Nd is arbitrarily set to the same as ^{204}Pb . As an example, Table 3 lists the initial

concentrations for the calculations that start 3.6 Gyr before present. Table 3 also lists radiogenic decay constants and heat production.

[27] For simplicity, a homogeneous initial composition is assumed for the cases studied here, although this model can also be used to treat a layered initial condition [Tackley and Xie, 2002].

2.3.5. Isotopic Fractionation

[28] The trace elements are partitioned between residue and melt at each melting event, prior to eruption, as follows. When partial melting occurs in a cell, concentrations are calculated by integrating over particles in that cell. The partitioning of trace elements between melt (new crust) and remaining solid is then calculated following Christensen and Hofmann [1994].

[29] In a melting event, basalt tracers may be erupted to the surface, while residue tracers do not change their position. All tracers in a cell that participates in a melting event constitute a sampling batch. The sampling volume V is simply the volume of that cell. The total concentration C^0 of a certain nuclide in the sampling batch is calculated as

$$C^0 = \frac{1}{V} \left(\sum_{i=1}^N a_i + \sum_{j=1}^M a_j \right) \quad (16)$$

where N is the number of basalt tracers and M is the number of residue tracers. The trace element concentration is fractionated between the melt (C_m) and the residue (C_r):

$$C_m = \frac{C_0}{(D + f(1 - D))} \quad (17)$$

$$C_r = C_m D \quad (18)$$

where D is the partition coefficient and f is the degree of melting, which is determined by the solidus and latent heat (equation (13)). Trace elements are redistributed to basalt and residue tracers according to

$$a_i = c_m f V / N = C_m / n_0 \quad i = 1, 2, 3, \dots, N \quad (19)$$

$$a_j = c_r V (1 - f) / M \quad j = 1, 2, 3, \dots, M \quad (20)$$

Table 3. Isotopes for Concentrations, Partition Coefficients, Relevant Decay Products, Decay Rate, and Heat Production Rate^a

Isotope	Current Concentration	3.6 Gyr B.P. Concentration	D	Daughter	Decay Rate, yr^{-1}	Heat, $\mu\text{W kg}^{-1}$
^{238}U	4.65×10^{13}	8.12×10^{13}	0.007	^{206}Pb	1.55×10^{-10}	95.0
^{235}U	3.37×10^{11}	1.17×10^{13}	0.007	^{207}Pb	9.85×10^{-10}	562.0
^{232}Th	1.82×10^{14}	2.18×10^{14}	0.007	^{208}Pb	4.95×10^{-11}	26.6
^{206}Pb	9.81×10^{13}	6.34×10^{13}	0.025			
^{207}Pb	8.09×10^{13}	6.95×10^{13}	0.025			
^{204}Pb	5.23×10^{12}	5.23×10^{12}	0.07			
^{147}Sm	7.85×10^{11}	8.03×10^{11}	0.09	^{144}Nd	6.54×10^{-12}	
^{143}Nd	2.69×10^{12}	2.67×10^{12}	0.07			
^{144}Nd	5.23×10^{12}	5.23×10^{12}	0.07			
^{40}K	4.12×10^{14}	3.03×10^{15}	0.01		5.54×10^{-10}	30.0

^aConcentrations are in atoms per gram. Radiogenic production of noble gases are not listed. Blank entries mean zero or none.

Between sampling events, the amount a^P of a radioactive parent nuclide and the amount a^D of a radioactive parent's daughter on a given tracer change according to

$$a^P(t) = a^P(t_0)e^{-\lambda(t-t_0)} \quad (21)$$

$$a^D(t) = a^D(t_0) + a^P(t_0)(1 - e^{-\lambda(t-t_0)}) \quad (22)$$

where λ is the decay constant and t_0 is the time of the last sampling of the tracer in a melting zone.

[30] Values of partition coefficients are also given in Table 3. As in the work by *Christensen and Hofmann* [1994], it is necessary to set the partition coefficient for Pb artificially much higher than that for U in order to produce HIMU material, as the processes that produce HIMU on Earth (e.g., addition of U by hydrothermal circulation, preferential removal of Pb in subduction zones) are not included in the model. These are further discussed in section 3.4.

2.3.6. Radioactive Decay and Heating

[31] Radioactive decay of U, Th and K produces a large part of the heat input in the model (the other is core cooling, as discussed in section 2.2). Thus the internal heating rate varies spatially and temporally according to the local concentration of heat producing isotopes of U, Th, and K. Table 3 lists the heat production rate and decay rate of these isotopes. This results in a volume-averaged internal heating rate that falls from ~ 60 to ~ 20 nondimensional units over the course of a calculation, where 1 is 2.7×10^{-13} W kg $^{-1}$.

2.3.7. Determining Isotopic Ages

[32] Isotope ratios evolve along different paths in the differentiated crust and residue because the ratio of parent/daughter is changed by fractionation. A mean age can be determined analytically from the isotope ratio arrays. Both Sm-Nd and U-Pb systems are tracked, and can be used to infer the mean age of chemical heterogeneities. Lead-uranium evolution has two parallel decay schemes, ^{238}U to ^{206}Pb and ^{235}U to ^{207}Pb , each of which is referred to the nonradiogenic isotope ^{204}Pb . Because the samarium-neodymium system involves only parent and daughter isotope (^{147}Sm to ^{143}Nd , with ^{144}Nd as the nonradiogenic isotope), it provides a much simpler way to determine the age.

[33] For the Pb system, determining age requires solving

$$f(x) = 137.88s(e^{0.155125x} - 1) - e^{0.98485x} + 1 = 0 \quad (23)$$

where s is the slope in $^{207}\text{Pb}/^{204}\text{Pb}$ – $^{206}\text{Pb}/^{204}\text{Pb}$ space and x is the age of interest in billion years. Some exemplary values of slope and age pairs are age of 1.8 Gyr when $s = 0.11$ and age of 2.0 Gyr when $s = 0.13$.

[34] The Sm-Nd system is simpler, with only one decay system, resulting in

$$t = \frac{1}{\lambda_{sm147}} \ln(1 + s) \quad (24)$$

where s is the slope in $(^{143}\text{Nd}/^{144}\text{Nd})$ – $^{147}\text{Sm}/^{144}\text{Nd}$ space. Some exemplary values are $t = 2.0$ Gyr, when the slope $s = 0.0131$.

[35] One drawback with the isochron equation (24) is that the parent/daughter ratio is not preserved in the basalts; additionally, the large spread of the data leads to large uncertainty in fitting a line. *Blichert-Toft and Albarède* [1994] used another more practical method to calculate the time interval necessary to obtain the $^{143}\text{Nd}/^{144}\text{Nd}$ range for a given range of $^{147}\text{Sm}/^{144}\text{Nd}$. The linearized equation of radioactive decay over a time interval ΔT can be written

$$\delta\left(\frac{^{147}\text{Sm}}{^{144}\text{Nd}}\right) = \frac{\delta\left(\frac{^{143}\text{Nd}}{^{144}\text{Nd}}\right)}{\lambda\Delta T} \quad (25)$$

where λ is the decay constant of ^{147}Sm , and $\delta(^{147}\text{Sm}/^{144}\text{Nd})$ and $\delta(^{143}\text{Nd}/^{144}\text{Nd})$ are the ranges in the $^{147}\text{Sm}/^{144}\text{Nd}$ ratio and the $^{143}\text{Nd}/^{144}\text{Nd}$ ratio, respectively. Using this method, the Nd age determined from the data in Figure 2 is around 1 Gyr for modern basalts and about 10 times smaller for Archean basalts [*Blichert-Toft and Albarède*, 1994].

2.4. Stretching of Mantle Heterogeneity

[36] In early mantle mixing studies [e.g., *Gurnis and Davies*, 1986b; *McKenzie*, 1979; *Christensen*, 1989; *Kellogg and Turcotte*, 1990], the amount of integrated strain that a heterogeneity experienced, i.e., how much it has been stretched, was used as the main criterion for deciding whether heterogeneities had mixed well in the mantle. For example, *Christensen* [1989] considered the mantle to be well mixed when 90 percent of heterogeneities are reduced to a thickness of less than $e^{-4} = \sim 1/55$ of their original size. A heterogeneity of initial thickness 7 km, such as subducted oceanic crust would then be reduced to a thickness of O(100 m), which might be too small for it to be identifiable as an individual magma source. This process is not adequately represented by the dispersion of initially bunched tracers, because when a heterogeneity that is initially represented by a bunch of N tracers is stretched by the flow, the tracers soon spread out into a line of separate individual tracers which then each retain their distinct signature of $1/N$ of the original heterogeneity's; that is, beyond the point at which tracers become separated, further stretching does not reduce their influence on isotopic signatures.

[37] In order to investigate the effect of further stretching, tracers are also treated as strain markers using the approach of *Kellogg and Turcotte* [1990], in which the aspect ratio and orientation of an initially circular (two-dimensional) strain ellipse are integrated along each tracer's path. To relate this to isotopic signatures some approximation of the effect of this stretching on a tracer's contribution is then necessary; some simple possibilities are now considered. The simplest option would be to ignore tracers with high strains when calculating isotope ratios, which could be done in postprocessing, but this has the disadvantage of not conserving mass. In order to conserve mass, it seems preferable to instead redistribute the isotopes from high-strain tracers to other tracers, during the calculation. This could be done locally, e.g., within a grid cell, or globally, recognizing that "blobs" become spread into thin lamellae or tendrils that may extend over wide regions. This redistribution, either local or global, is adopted in some of the presented calculations, and occurs once the strain on a tracer reaches a preset threshold, different values of which are

tested. More sophisticated techniques are also possible, notably the statistical approach of *Kellogg et al.* [2002] and will be implemented in the future.

[38] Tracer age is also tracked, which is here defined as the time since the last melting or stretching-induced resetting, or the beginning of the calculation if the tracer has never participated in melting.

3. Results

3.1. Cases and Initial Condition

[39] Many cases have been calculated, with different combinations of start time, method (if any) of treating high-strain tracers, and deep-mantle chemical density contrast. The start time is either 4.5 Gyr B.P. (before present) or, following *Christensen and Hofmann* [1994], 3.6 Gyr B.P. When used, the strain threshold for redistributing isotopes from high-strain tracers is varied from 10 to 1000 but is typically 60 (following *Christensen* [1989]), and either local (grid cell) or global redistribution is tested. For most cases it is assumed that the “garnet-pyroxene” component (effectively, basalt/eclogite) is denser in the deep mantle (curve GtPxReference in Figure 3), but for some cases the possibilities that this component is neutrally dense (curve GtPxNeutral) or less dense (curve GtPxBuoyant) are considered.

[40] Temperature is initialized to an adiabat, with error function thermal boundary layers of nondimensional thickness 0.03 at top and bottom and small random perturbations in temperature. Care is taken to choose the initial adiabat so that the temperature is everywhere lower than the solidus to avoid a huge pulse of melting in the first time step; a potential temperature of 1800 K accomplishes this.

[41] The presentation starts by considering the evolution of 2-D fields from typical cases, then focuses on issues of effective isotopic age inferred from Pb-Pb isochrons.

3.2. Time Evolution

[42] The time evolution of temperature, composition, isotope ratios, and age is illustrated for a typical case, which runs for 3.6 Gyr and has isotope redistribution at a strain of 60, in Figure 4. Times of 1, 2, and 3 Gyr after the start are shown.

[43] Partial melting rapidly causes the formation of a crust and complementary depleted layer beneath it (Figure 4b). Yielding in the lithosphere allows subduction to take place (Figure 4a), and the crust and residue are carried to the CMB region, where some fraction of the subducted crust segregates into a layer, which thickens with time (Figures 4b, 4h, and 4n). Although the crust is compositionally buoyant near the surface, below about 60 km it transforms to the denser eclogite phase, resulting in slabs that are compositionally neutrally buoyant.

[44] The two-component phase transitions around 660–720 km depth interact with compositional variations to cause partial stratification [*Ogawa*, 2000; *Fleitout et al.*, 2000; *Tackley*, 2002a; *Xie and Tackley*, 2004]. Depleted harzburgite from subducted slabs is trapped beneath this region as it rises from the deep mantle (Figures 4h and 4n). Sometimes the transition zone contains crust-enriched components.

[45] In the first age plot (Figure 4c), red material has never melted, while the compositionally defined lithosphere (i.e., crust and residue) appears blue and green. The “young” material (slabs) initially falls to the CMB, and then some fraction of it rises, consistent with the findings of *Ferrachat and Ricard* [2001]. After 2.0 Gyr (Figure 4i), most of the mantle has acquired a younger age but some old material still exists, scattered around the mantle, i.e., not preferentially located at any particular depth. After 3.0 Gyr (Figure 4o), only small amounts of old material remain, with the lower mantle appearing to be older, on average, than the upper mantle.

[46] U/Pb (μ) is high in crust and low in residue because lead is assumed to be more compatible than uranium, as explained in section 2.3.5. The deep layer of subducted crust thus has high- μ , although the low μ in residue appears more pronounced (Figures 4d, 4j, and 4p). High (radiogenic) $^{206}\text{Pb}/^{204}\text{Pb}$ develops in high- μ regions such as the layer above the CMB, and appears more pronounced than low $^{206}\text{Pb}/^{204}\text{Pb}$ residue (Figures 4e, 4k, and 4g).

[47] The Sm-Nd isotopic ratios display similar distributions, although with the opposite sense because the radiogenic parent element Sm is less incompatible than the daughter element Nd. Thus $^{147}\text{Sm}/^{144}\text{Nd}$ is low in the crust and high in the residue. The dense layer above the CMB has low $^{147}\text{Sm}/^{144}\text{Nd}$ (Figures 4f, 4l, and 4r). Resultantly, $^{143}\text{Nd}/^{144}\text{Nd}$ (not shown) becomes low in the dense layer.

[48] The time evolution of various model diagnostics for a 4.5 Gyr calculation is plotted in Figure 5. Heat flows have been scaled to a spherical Earth, assuming, as found by *Van Keken* [2001], that the heat fluxes in rescaled cylindrical geometry are similar to those in full spherical geometry. The total surface heat flow (plotted using a 500 Myr running average to emphasize the long-term trend) decreases from about 100 TW to 20 TW over the course of the calculation, the present value being lower than the estimated mantle heat flow of 34 TW, a perennial problem in mantle thermal evolution calculations that has been the subject of some interesting recent hypotheses [*Conrad and Hager*, 1999; *Korenaga*, 2003]. The CMB heat flow drops to around zero by 2 Gyr in the calculation due to rapid core cooling and the blanketing of the core by hot, dense material enriched in heat-producing elements. The evolution of core heat flux in a differentiating mantle is the subject of a recent study by *Nakagawa and Tackley* [2004], from which it appears that when a more complete core model that includes the energy release associated with inner core growth is used, the CMB heat flow does not fall to zero but can remain high enough to drive the geodynamo throughout Earth’s evolution. The main effect of having too little core heat flow is likely to make the layer of dense material more stable than it should be.

[49] It is instructive to decompose the surface heat flow into conductive and magmatic components (Figure 5a). While the conductive heat flow remains in the range 20–30 TW throughout model history, magmatic heat flow is low in recent history but exceeded conductive heat flow during the first 2 Gyr. Low present-day magmatic heat flow is realistic. The present-day oceanic crust production rate is about 6×10^{13} kg yr $^{-1}$ [*Stacey*, 1992; *Coltice and Ricard*, 1999]. The latent heat associated with melting this much material is about 1 TW. The resulting magma

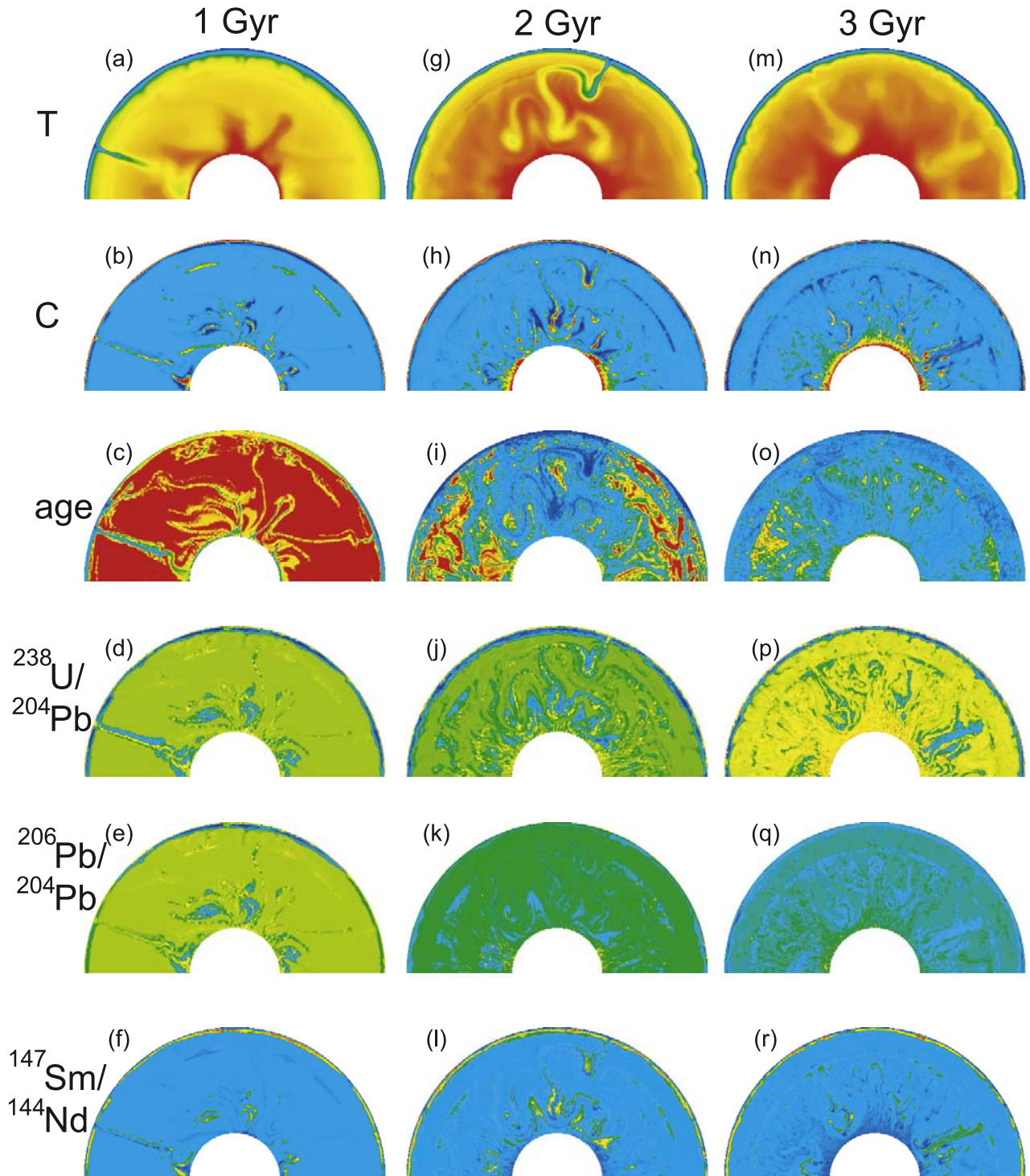


Figure 4. Temperature, composition, tracer age, and isotopic state for a 3.6 Gyr case at (a–f) $t = 1.0$ Gyr, (g–l) $t = 2.0$ Gyr, and (m–r) $t = 3.0$ Gyr. In Figures 4a, 4g, and 4m, temperature field ranges from 300 K (blue) to 3000 K (red). In Figures 4b, 4h, and 4n, composition ranges from $C = 0$ (blue) to $C = 1$ (red). Tracer age ranges from $t = 0$ (blue) to $t = 1.0$ Gyr (red) for Figure 4c, from $t = 0$ (blue) to $t = 2.0$ Gyr (red) for Figure 4i, and from $t = 90$ Myr (blue) to $t = 3.0$ Gyr (red) for Figure 4o. The $^{238}\text{U}/^{204}\text{Pb}$ (μ) ratio ranges from 0.19 (blue) to 23.3 (red) for Figure 4d, from 0.16 (blue) to 21 (red) for Figure 4j, and from 0.17 (blue) to 15.3 (red) for Figure 4p. The $^{206}\text{Pb}/^{204}\text{Pb}$ ratio ranges from 12.9 (blue) to 15.3 (red) for Figure 4e, from 14.3 (blue) to 18.4 (red) for Figure 4k, and from 16.0 (blue) to 20.5 (red) for Figure 4q. The $^{147}\text{Sm}/^{144}\text{Nd}$ ratio ranges from 0.1298 (blue) to 0.2422 (red) for Figure 4f, from 0.1285 (blue) to 0.2310 (red) for Figure 4l, and from 0.13 (blue) to 0.233 (red) for Figure 4r.

is removed hot, and after solidifying to form crust, cools rapidly to the surface temperature. Assuming that it cools by about 1000 K, the associated heat release is 2.3 TW, bringing the total magmatic present-day heat flux to 3.3 TW, about 10% of the mantle heat loss. The model magmatic heat flow plotted in Figure 5 is the sum of these two contributions. It is not known how Earth's magmatic heat flow varied in the past, but this model

suggests that it may have been important and should be further studied.

[50] Surface velocity, crustal production and temperature are shown for three different cases that differ only in the treatment of high strain tracers: either no treatment, erasure at a strain of 60, or at a strain of 10. Surface velocity (RMS) fluctuates in the range $0.5\text{--}5\text{ cm yr}^{-1}$, with the fluctuations correlated with magmatism. The first couple of fluctuations are correlated for the three cases, when then diverge but follow a similar long-term trend. Although there is a general decrease with time, it is a much weaker variation than the $(\text{heat flux})^2$ relation commonly assumed in parameterized models [e.g., *Davies, 2002; Morgan and Morgan, 1999*]. In the last ~ 2 Gyr, velocities of around 1 cm yr^{-1} were typical, about a factor of 3 lower than the present-day poloidal RMS plate velocity [*Lithgow-Bertelloni et al., 1993*].

[51] The integrated amount of crust produced, expressed as a fraction of mantle volume, is plotted in Figure 5c. As expected, this grows rapidly at first, with a gradient that decreases with time. By the end of the model calculation, the total volume of crust produced is about 34% of mantle volume. This is larger than the total amount of crustal material in the model, indicating that some crust has melted more than once and suggesting that all material has melted; however the latter is not correct due to the stochastic nature of material transport through the melting region: some material has melted multiple times, whereas other material has never melted. This is compared to idealized parameterized models of Earth evolution in section 3.4.2. All three cases end with a similar total crustal production.

[52] Volume-averaged temperature initially increases but then shows a long-term decrease with time. This volume average includes the accumulating layer of hot material at the base of the mantle, so is not a direct indication of the potential temperature in the upper mantle, which is the usual quantity that is considered in thermal evolution models.

[53] The crustal production rate, averaged for the three cases (Figure 5e) is roughly constant over the last 1.5 Gyr but was higher before then. Also plotted are two theoretical models that are discussed in section 3.4.2; the overall trend appears to be between these two models.

3.3. Effect of Chemical Buoyancy

[54] In Figure 6, the final (present-day) state of the case in Figure 4 is contrasted with two other cases that have different compositional buoyancy in the deep mantle. The dense crustal layer above the CMB with the default com-

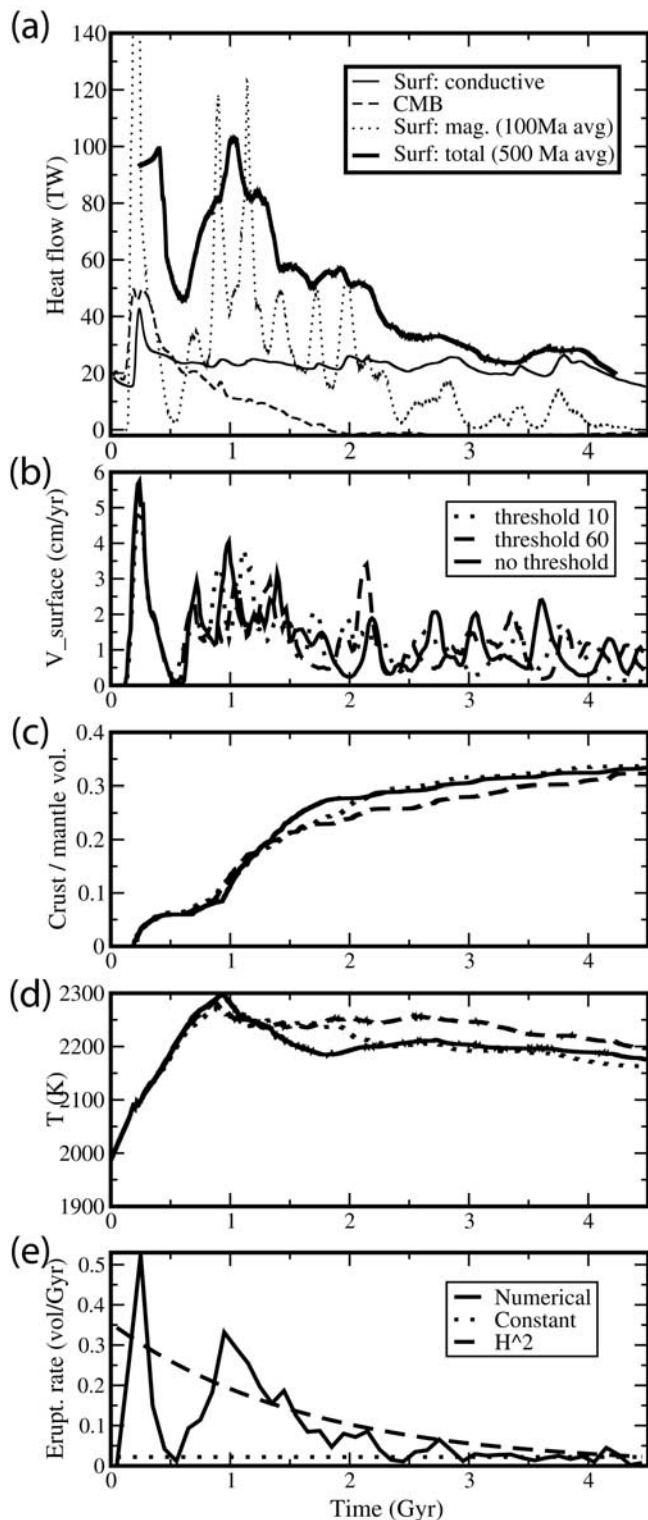


Figure 5. Time evolution of various diagnostics for 4.5 Gyr calculations. (a) Surface and CMB heat flow for a case with strain threshold 10, scaled to a spherical planet, showing CMB (dashed), surface conductive (solid), surface magmatic (dotted), and surface total (bold indicates averaged over a 500 Myr sliding window). (b) RMS surface velocity for three cases. (c) Integrated crustal production as a fraction of mantle volume for three cases as in Figure 5b. (d) Volume-averaged temperature for three cases as in Figure 5b. (e) Crustal production (eruption) rate in mantle volumes per Gyr, averaged over the three cases in 100 Myr bins, and compared to theoretical models (dotted and dashed lines).

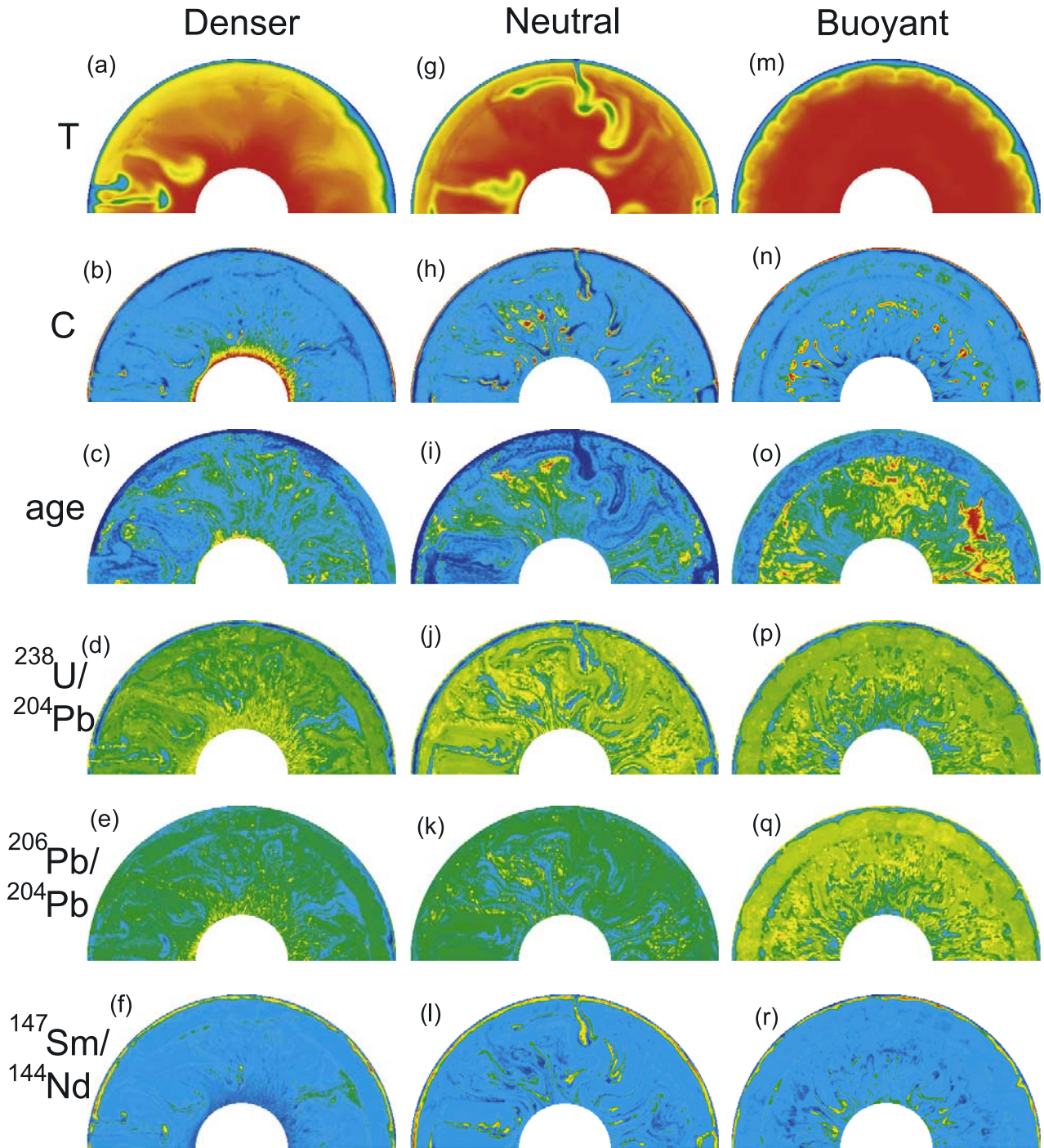


Figure 6. Temperature, composition, tracer age, and isotopic state at the end of 3.6 Gyr cases with (a–f) crust dense at CMB, (g–l) neutrally buoyant crust at CMB, and (m–r) buoyant crust at CMB. In Figures 6a, 6g, and 6m, temperature field ranges from 300 K (blue) to 3000 K (red). Figures 6b, 6h, and 6n, composition ranges from $C = 0$ (blue) to $C = 1$ (red). Tracer age ranges from $t = 0$ (blue) to $t = 3.33$ Gyr (red) for Figure 6c, from $t = 0$ (blue) to $t = 3.6$ Gyr (red) for Figure 6i, and from $t = 100$ Myr (blue) to $t = 3.6$ Gyr (red) for Figure 6o. The $^{238}\text{U}/^{204}\text{Pb}$ (μ) ratio ranges from 0.17 (blue) to 16.4 (red) for Figure 6d, from 0.24 (blue) to 15.3 (red) for Figure 6j, and from 0.13 (blue) to 16 (red) for Figure 6p. The ratio $^{206}\text{Pb}/^{204}\text{Pb}$ ratio ranges from 16.8 (blue) to 20.9 (red) for Figure 6e, from 16.7 (blue) to 20.9 (red) for Figure 6k, and from 15.6 (blue) to 20.9 (red) for Figure 6q. The $^{147}\text{Sm}/^{144}\text{Nd}$ ratio ranges from 0.127 (blue) to 0.232 (red) for Figure 6f, from 0.13 (blue) to 0.22 (red) for Figure 6l, and from 0.129 (blue) to 0.230 (red) for Figure 6r.

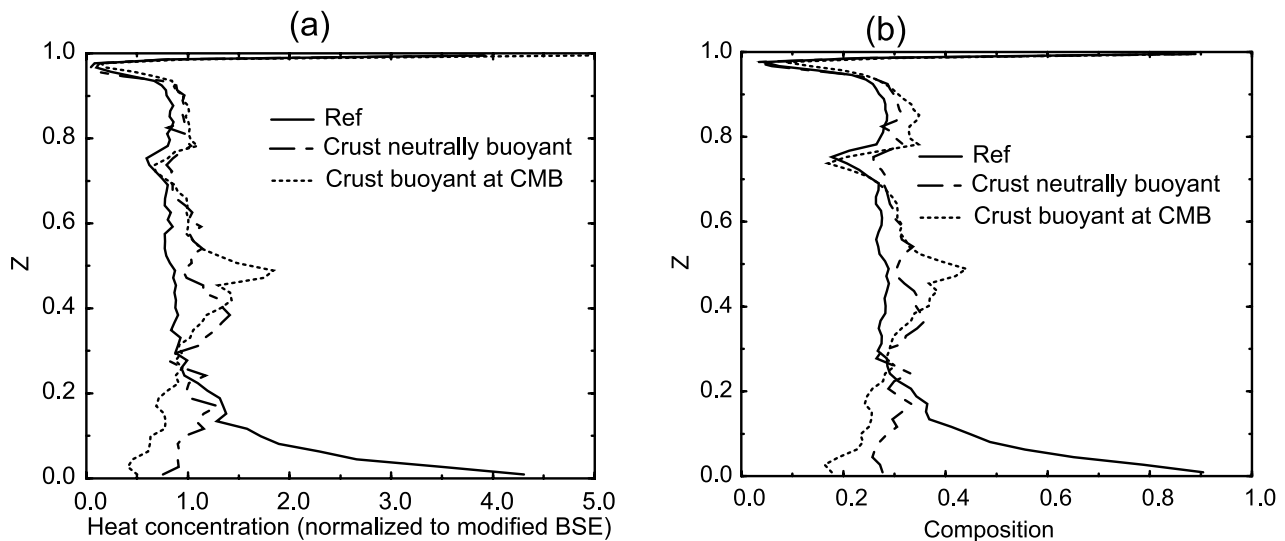


Figure 7. Horizontally averaged radial profiles of (a) radiogenic heat production relative to mean and (b) composition.

positional density profiles (i.e., crust is dense in the deep mantle) is not a smooth layer, as is often assumed in studies where such a layer is inserted a priori [e.g., *Montague et al.* 1998], but instead the topography of the layer is complex, with roughness, spikes, and patches at its top (Figure 6b). This layer is enriched in the (incompatible) heat-producing elements uranium, thorium, and potassium. Despite this, the layer is not incredibly hot, mainly because the CMB temperature has dropped to a relatively low value due to the use of a very simple core thermal parameterization that does not account for the latent heat release of inner core growth, as is done in other recent models [*Nakagawa and Tackley, 2004*]. Broad hot upwellings (not narrow plumes) rise from this layer (Figure 6a). Little primordial material is visible in the age distribution (Figure 6c), although the lower mantle appears, on average, to be “older” than the upper mantle. Distributions of μ , $^{206}\text{Pb}/^{204}\text{Pb}$ and $^{147}\text{Sm}/^{144}\text{Nd}$ (Figures 6e–6f) are similar to those discussed previously.

[55] When crust is neutrally buoyant at the CMB (Figures 6g–6l), subducted slabs reside temporarily at the base of the mantle until they warm up sufficiently to rise, and the lower mantle is a heterogeneous mixture of crust, residue and unmelted components (Figures 6h–6i). In some ways this appears similar to the penetrative convection model developed by *Silver et al.* [1988], but in this case the slabs are compositionally neutrally buoyant rather than positively buoyant and so tend to mix into the lower mantle rather than rising back into the upper mantle. The distribution of age (Figure 6i) is also heterogeneous perhaps with a greater tendency for older material to be in the lower mantle. Isotopic ratios (Figures 6j, 6k, and 6l) also show great spatial heterogeneity with no clear preferential location for any component.

[56] When crust is buoyant in the deep mantle (Figures 6m–6r), blobs of former crustal material tend to accumulate in the midmantle where they are neutrally buoyant (Figure 3), while depleted residuum tends to gravitate to the deepest mantle, and is also preferentially found below the

660 km discontinuity (Figure 6n). The temperature field (Figure 6m) indicates that plate tectonics has ceased; in fact, no plate tectonics or melting occurred for the last approximately billion years of this case. As a result of this, the lower mantle is distinctly older than the upper mantle (Figure 6o). As expected, isotopic ratios indicate depletion in the deepest mantle where the residue accumulates (Figures 6p–6r).

[57] The crustal density profile has a strong effect on radial profiles of mean composition and heat production. Compositional profiles (Figure 7b) show a basaltic crust underlain by depleted residue in all cases; additionally all cases show a depleted zone just below the 660 km discontinuity. The dense crust case shows a crustal layer above the CMB, whereas the buoyant crust case is slightly depleted in this region with a crust-enriched region in the mid lower mantle.

[58] Profiles of radiogenic heat production (Figure 7a) naturally reflect the composition profiles (because the incompatible heat-producing elements (HPE) partition into the crust) but with larger amplitude. Of particular interest is the case with a basal layer of subducted crust, in which heat production in it is up to 4.5 times higher than the global average. This is qualitatively but not quantitatively consistent with the proposal of *Coltice and Ricard* [1999], who proposed that sequestering of $\sim 1/3$ of Earth’s HPE into such a deep crustal layer may account for the very low concentration in the MORB source. In the calculation presented here, the HPE concentration in the rest of the mantle is certainly lower but not by the large factor necessary to match the MORB source. This is because the concentration of HPE in the crust is at least two times lower than that proposed by *Coltice and Ricard* [1999], which is about ten times the BSE concentration. This may be due to an unrealistically high degree of melting in the present calculations (compared to the ~ 8 – 10% though to be appropriate for present-day MORB), which results in a lower than realistic concentration of HPE in the crust. Future work must attempt to match Earth’s parameter range more precisely in order to address the proposal of *Coltice*

and Ricard [1999]. As it is, about 6.3 TW of heat is stored in the basal layer. If the concentration of the average mantle is subtracted, then this layer can sequester 3.1 TW of “missing” heat.

3.4. Isotope Ratios

[59] In Figure 8, $^{207}\text{Pb}/^{204}\text{Pb}$ – $^{206}\text{Pb}/^{204}\text{Pb}$ isotope ratio plots (with Sm–Nd shown for one case) are compared for various cases, with particular attention paid to the effective age obtained from the least squares slope in $^{207}\text{Pb}/^{204}\text{Pb}$ – $^{206}\text{Pb}/^{204}\text{Pb}$ space (section 2.3.7). Note that although the slope has the dimension of age, the continuous differentiation of the Earth means that it cannot be interpreted as the age of a single differentiation event [Albarède, 2001; Hofmann, 1997; Allègre et al., 1980]. Even so, it is an important quantity that can be compared between model and Earth. Each point on the diagram corresponds to one sampling cell, of which there are normally 256×64 (roughly 60×45 km).

[60] The Pb–Pb diagram for a case that runs for 4.5 Gyr with reference parameters (Figure 8a) displays extreme scatter, larger than that observed in real data, and a much too large slope and Pb–Pb age of 3.39 Gyr.

[61] This large age is not surprising, because the rate of melting is much higher earlier in the evolution, so early differentiating material dominates the isotopic signature. Additionally, early differentiated material has developed a more radiogenic signature so influences the least squares fit more than recently differentiated material. This finding is consistent with previous attempts at modeling lead isotope ratios starting from 4.5 Gyr ago that obtained unrealistically high slopes in $^{207}\text{Pb}/^{204}\text{Pb}$ – $^{206}\text{Pb}/^{204}\text{Pb}$ space [Allègre et al., 1980; Armstrong and Hein, 1973]. Christensen and Hofmann [1994] attributed this to the rapid decay of ^{235}U into ^{207}Pb in the early stage of the model, also finding that the early differentiation has a strong effect on the isotopic signatures at the end of the run. Thus they chose to start their models 3.6 Gyr ago with uniform Pb composition, which assumes that any earlier differentiation in the mantle has been completely homogenized by the convection.

[62] There are several possible explanations for the discrepancy between model and data that are now investigated. These are that HIMU material may not have been subducted into the mantle prior to 2.0–2.5 Gyr B.P., that there is not enough melting in the model, that stretching of heterogeneities is inadequately represented, that the “sampling volume” over which isotopic ratios are calculated is incorrect, that the deep-mantle density of crustal material is incorrect, or that the Pb–Pb slope is made artificially large by noise associated with tracer discretization.

3.4.1. HIMU Not Produced Early on

[63] One possible solution for this discrepancy is that HIMU material did not enter the mantle before 2.0–2.5 Gyr ago, for which there are two possible explanations. One of these is that higher subduction zone temperatures in the past may have caused essentially all Pb, U, and other trace elements to be stripped from the subducted crust by melting [Martin, 1986]. Supporting this explanation is eclogite xenoliths from the upper mantle under western Africa that are highly depleted in incompatible elements and have been interpreted as the melting residue of Archean subducted crust [Barth et al., 2001]. Another possible explanation is

that the HIMU end-member was not produced prior to the rise in atmospheric oxygen about 2.2 Gyr ago. In this latter scenario, HIMU is produced by addition of continental U to oceanic crust by hydrothermal circulation at ridges [Michard and Albarède, 1985; Elliott et al., 1999], with efficient stripping of U from continents being accomplished by an oxygen-rich atmosphere oxidizing U to its 6+ state [Holland, 1984, 1994]. This is not the only process that has been proposed to produce HIMU: the other is preferential stripping of Pb (relative to U) from the subducted crust to the overlying mantle in subduction zones [Newsom et al., 1986; Hofmann, 1988; Chauvel et al., 1995]. It is possible that both of these processes may operate.

[64] In the presented numerical model, as in that of Christensen and Hofmann [1994], HIMU is produced by artificially changing the partition coefficients of U and Pb so that they fractionate on melting. In order to evaluate the effect of it not being produced prior to some point in the past, we have run cases in which the U and Pb partition coefficients are set equal for the first part of the model run, then changed to their default values at a specified point in the past. A case for which this transition is 2.5 Gyr before present is illustrated in 7b; the isotopic age of 1.75 Gyr and the spread of values are both reasonably Earth-like. When the transition occurs at 2.0 Gyr before present (not illustrated) an isotopic age of 1.4 Gyr is obtained. Thus, from a modeling perspective a lack of HIMU production prior to 2–2.5 Gyr ago is an appealing mechanism for explaining the effective age of the Pb–Pb isotope diagrams, although it needs to be shown that this fits other isotope systems too.

[65] A variant on this theme is to assume that the mantle was homogeneous due to rapid mixing before some point in the past, and start the calculation from that point. This provided a justification for Christensen and Hofmann [1994] to start their published models from 3.6 Gyr B.P. A case with the reference parameters starting at 3.6 Gyr B.P. is shown in Figure 8g. The scatter is greatly reduced (although still larger than Earth-like) as is the slope, which gives an effective age of 2.52 Gyr. It is necessary to add some additional effect to get down to realistic ages, as exemplified in sections 3.4.2–3.4.4.

3.4.2. Unrealistic Melting History?

[66] One method for elimination of old heterogeneity is by remelting it, so the possibility must be explored that the presented models exhibit insufficient melting in the past. Simple box models are here used for this exploration. In these, the mantle is considered to be a box with a uniform average age. During each time interval melting removes a small fraction of material with the mean age, resets its age to zero, and replaces it in the box. The calculation is initialized 4.5 Gyr ago with an age of zero following which the age evolves as

$$\frac{d\langle\text{age}\rangle}{dt} = 1 - \frac{\langle\text{age}\rangle}{\text{volume}} \frac{dm}{dt}(t) \quad (26)$$

where the key inputs are the time history of melting $dm/dt(t)$ and the volume. Three idealized scenarios are tested for the time history of melting, i.e., the time history of oceanic crustal production: (1) constant at the present-day value of about 6×10^{13} kg yr⁻¹ [Stacey, 1992; Coltice et al., 2000], (2) larger in the past proportional to the square

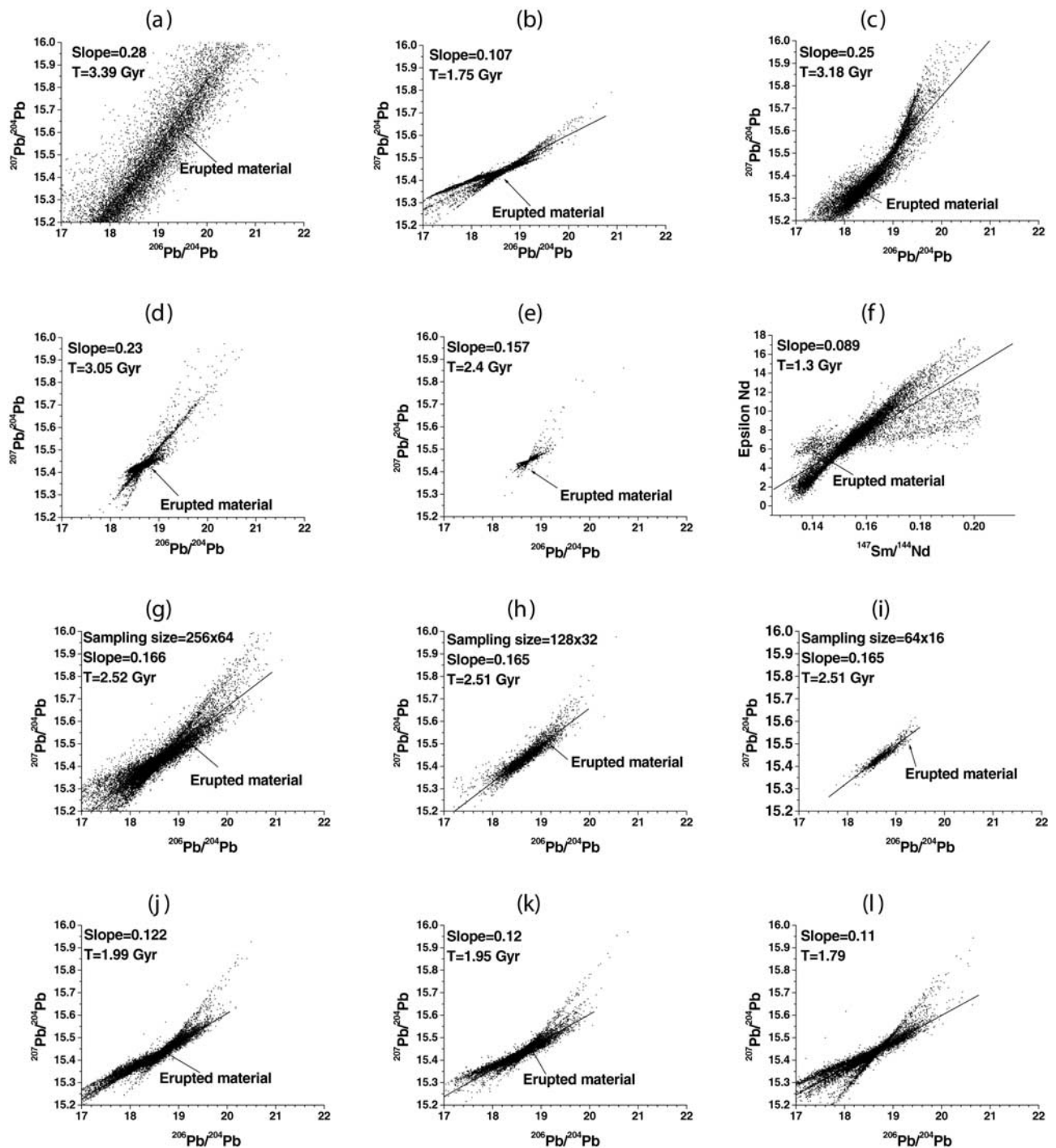


Figure 8. Pb-Pb and Nd-Sm isotope diagrams for the whole domain with the arrow lines indicating the average composition of erupted magmas and the sloping line being a least squares fit of the points. Pb ratios for 4.5 Gyr cases with reference parameters and (a) no effects, (b) no fractionation between U and Pb prior to 2.5 Gyr before present, (c) strain threshold 60 and local isotope redistribution, (d) strain threshold 60 and global isotope redistribution, (e) strain threshold 10 and global redistribution. Pb ratios for 3.6 Gyr cases with reference parameters except (f) Nd ratios, (g) 256×64 sampling cells ($\sim 60 \times 45$ km), (h) 128×32 sampling cells ($\sim 120 \times 90$ km), (i) 64×16 sampling cells ($\sim 240 \times 180$ km), (j) strain threshold of 60, (k) threshold 60, crust neutrally buoyant at CMB, and (l) threshold of 60, crust buoyant at CMB.

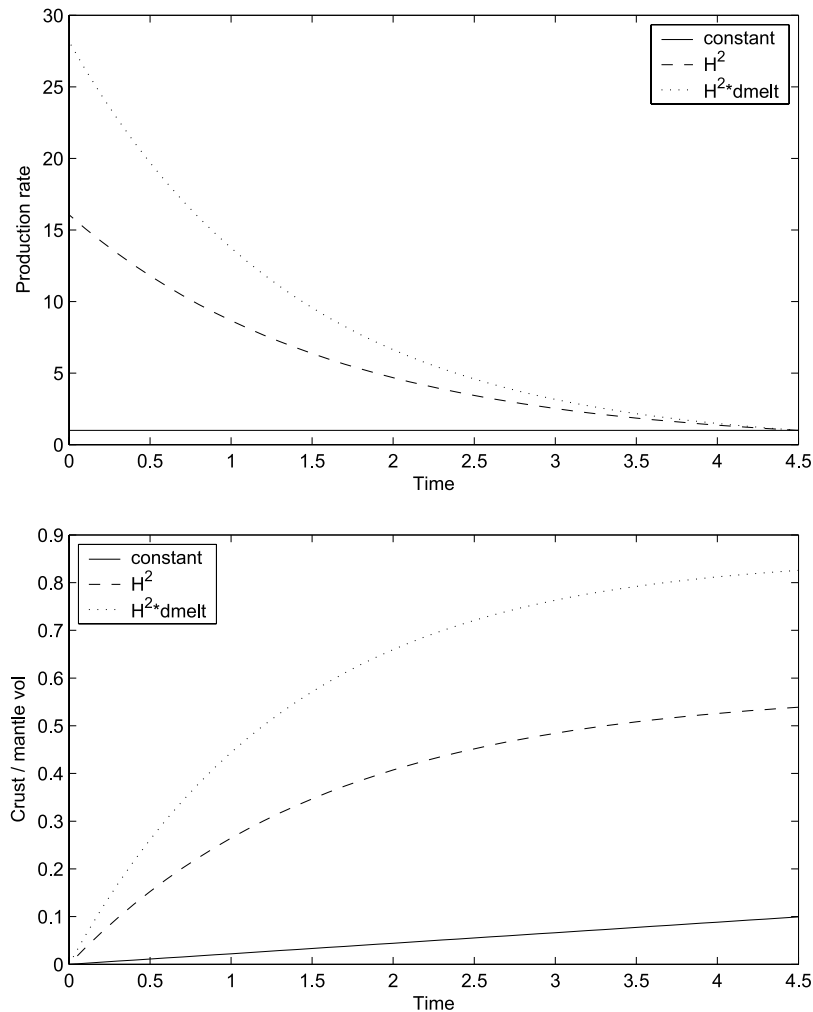


Figure 9. (top) Oceanic crust production rate and (bottom) integrated production versus model time for an idealized box model. The different lines correspond to different assumptions, as labeled.

of mantle heating rate [Davies, 2002; Morgan and Morgan, 1999], with the different radiogenic elements here lumped together with an average half-life of 2.247 Gyr, and (3) same as assumption 2 but also proportional to the depth of melting, which is assumed to be 80 km at present and increase by 1 km for every 3 K mantle temperature increase; mantle temperature is assumed to instantaneously self-adjust such that convection transports the produced heat, with mantle viscosity changing by an order of magnitude per 100 K temperature change. The melting histories resulting from these assumptions are plotted in Figure 9. Oceanic crust production rate decreases by a factor of 16 for assumption 2 and 28 for assumption 3. The integrated amount of crust produced climbs linearly to 0.1 mantle volumes for constant crustal production and climbs curvedly to 0.53 or 0.82 for the other assumptions. (This does not mean that crust makes up 82% of the mantle but that crustal material has melted several times during Earth history.) These idealized curves can be compared to the results of the numerical calculation (Figure 5c). The numerical results display a curved melting history with the total production falling between the constant and H^2 idealiza-

tions, at 0.34 mantle volumes. Melting rate (Figure 5e) is generally bracketed by the constant and heating rate squared assumptions.

[67] A key input parameter is the volume of mantle material that carries the isotopic signature which, crudely speaking, is the “crustal” or “basaltic” component. The degree of partial melting that produces oceanic crust on Earth is about 10%, so one possibility is that this volume should be 10% of mantle volume. Another approach, which leads to the same answer, would be to use the whole mantle volume but increase the melting rate by a factor of 10 to account for all of the material in the source region that is affected by melting and thus has its isotopic signature reset. However, although the fraction of melting below present-day spreading centers is about 10%, mantle material is capable of producing more and may well have done so in the past, in which case a number above 10% would be appropriate. In the numerical models, for example, the basaltic component makes up 30% of mantle volume.

[68] Results of the calculation are given in Table 4. An appropriate mean age of less than 2 Gyr is obtained only for the most extreme combination of inputs, i.e., basalt fraction $b = 0.1$ and a melting rate that increases rapidly going into

Table 4. Mean Mantle Age From Box Model Calculations^a

Model	$b = 0.1$	$b = 0.2$	$b = 0.3$
Constant	2.87	3.56	3.84
H^2	1.82	2.54	2.97
H^2d	1.65	2.29	2.70

^aThe parameter b is the basalt fraction of the mantle. See text for model descriptions.

the past. This implies much more frequent remelting than in the present numerical calculations, in which $b = 0.3$ and the melting history is intermediate between the constant and H^2 histories, consistent with the box model mean age range of 3.0–3.8 Gyr. Previous studies have assumed more frequent remelting. The previous numerical calculations of *Christensen and Hofmann* [1994] assumed $b = 0.125$ and a constant melting rate, which combined led to melting “statistically 90% of basalt in 1.36 Gyr.” Likewise, a recent parameterized study [*Kellogg*, 2004] assumed a mean remelting time of 1.25 Gyr.

[69] In summary, it is somewhat plausible that remelting could account for the difference between model and Earth, and this has been an important factor in previous modeling efforts, but it requires a steep increase in melting rate going back into the past, which is not obtained in the numerical model. A caution is that these ages are not directly comparable to Pb-Pb isotopic ages.

3.4.3. Insufficient Treatment of Strain

[70] As discussed in section 2.4, the stretching of heterogeneities into thin lamellae and tendrils that are no longer identifiable as individual magma sources has often been considered to be the main way that the signature of such heterogeneities is erased, but a tracer treatment of compositional heterogeneity does not adequately represent stretching beyond the point at which a blob is stretched into a line of tracers. Thus the effect of additional stretching is here approximated by resetting a tracer’s isotopic composition once it has reached a predetermined integrated strain. Specifically, this resetting is done by setting the tracer’s composition to the average composition of surrounding tracers, and (to conserve mass) redistributing trace elements in the process. The “surrounding tracers” are either those in the local sampling area (grid cell), or all tracers.

[71] In Figure 8c the strain threshold is set to 60 (similar to the criterion used by *Christensen* [1989] to determine well-mixed material) with local isotope redistribution. The main effect of this (compared to Figure 8a) is to greatly reduce the amount of scatter in the data, with a slight effect on the slope, bringing the age down to 3.18 Gyr. The reason for the relatively small effect on slope is presumably that extreme signatures are not completely eliminated, but rather, averaged over several tracers, which reduces the spread but not the trend. Redistributing isotopes globally (Figure 8d) further reduces the scatter and slope, but the effective age of 3.05 Gyr is still much too large. One possibility is, of course, that this strain threshold is too large, so in (Figure 8e) a strain of 10 with global redistribution is tried. Again, the scatter is further reduced, now to less than Earth-like, and the slope too (effective age = 2.4 Gyr), although the lack of a clear lineation in the data makes slope calculation less reliable. Thus it appears that im-

proved strain treatment cannot, by itself, reduce the age to the correct range: another effect is needed. Using a 3.6 Gyr run time is one possibility: Figure 8j shows a case that combines a 3.6 Gyr run time with strain threshold of 60, which leads to the correct scatter and slope of 1.99 Gyr.

[72] This can be further analyzed using histograms showing the age distribution of heterogeneities and the relationship between strain and age (Figure 10). With a 4.5 Gyr run time (Figure 10a), there is a large peak at around 2.8–3.6 Gyr, corresponding to the peak in surface magmatism at the corresponding elapsed time (Figure 5); the vast majority of tracers have ages of more than 2 Gyr. The log of the geometric mean strain increases approximately linearly with time, indicating exponential stretching, consistent with some previous studies [*Christensen*, 1989; *Kellogg and Turcotte*, 1990; *du Vignaux and Fleitout*, 2001]. With a 3.6 Gyr run time (Figures 10c and 10d), the distribution is naturally shifted to younger ages, but with peaks at around 2.4 and 3.5 Gyr, about 50% of the tracers have ages larger than 2.0 Gyr; the Pb-Pb isotopic age for this case is 2.52 Gyr (Figure 8g). As older tracers tend to have higher strains, ignoring high strain tracers in the plotting procedure biases the age distribution to younger ages, as shown in Figures 10e and 10f, where tracers with strains greater than 100 are ignored. Maximum strain (Figure 10f) is, of course, truncated at the threshold value, and the average strain for older tracers is reduced compared to nontruncated distributions. Resetting of high-strain tracers during the calculation has a similar effect, as shown in Figures 10g and 10h, which has a strain threshold of 60, leading to a Pb-Pb age of 1.99 Gyr (Figure 8j). Comparison of age distributions with Pb-Pb ages indicates that most heterogeneities are younger than the Pb-Pb age of the ensemble, consistent with the results of *Allègre and Lewin* [1995].

[73] It is useful to compare the mixing rate obtained here with previous estimates for whole mantle convection, which have mostly been based on stretching, although some are based on spatial dispersion of initially bunched tracers [*Olson et al.*, 1984]. Using idealized kinematic models, *Kellogg and Turcotte* [1990] estimated a mixing time of 960 Myr to reduce the length scale by 6–7 orders of magnitude. Using numerical convection models, however, *Christensen* [1989] obtained a longer mixing time of 1500–2000 Myr, even with a much less stringent criterion, i.e., reducing 90% of heterogeneities to less than 1/50th of their initial size. The present calculations are most consistent with these latter estimates: in Figure 10 the average strain reaches 50 in about 2 Gyr; analysis indicates that the median strain curve has the form of $\exp(1.81t)$, where t is in Gyr. It is possible that this time estimate should be reduced by a factor of about 3 to account for higher plate velocities in the real Earth.

3.4.4. Inappropriate Sampling Volume?

[74] Sampling volume, i.e., the size of the region over which isotopic signatures are calculated by integration of trace element compositions of tracers, may have an effect on the resulting isotope diagrams. To test this, Pb-Pb diagrams are shown for three different sampling volumes, corresponding to 256×64 cells, 128×32 cells, or 64×16 cells, in Figures 8g, 8h, and 8i, respectively. Note that these are for 3.6 Gyr calculations.

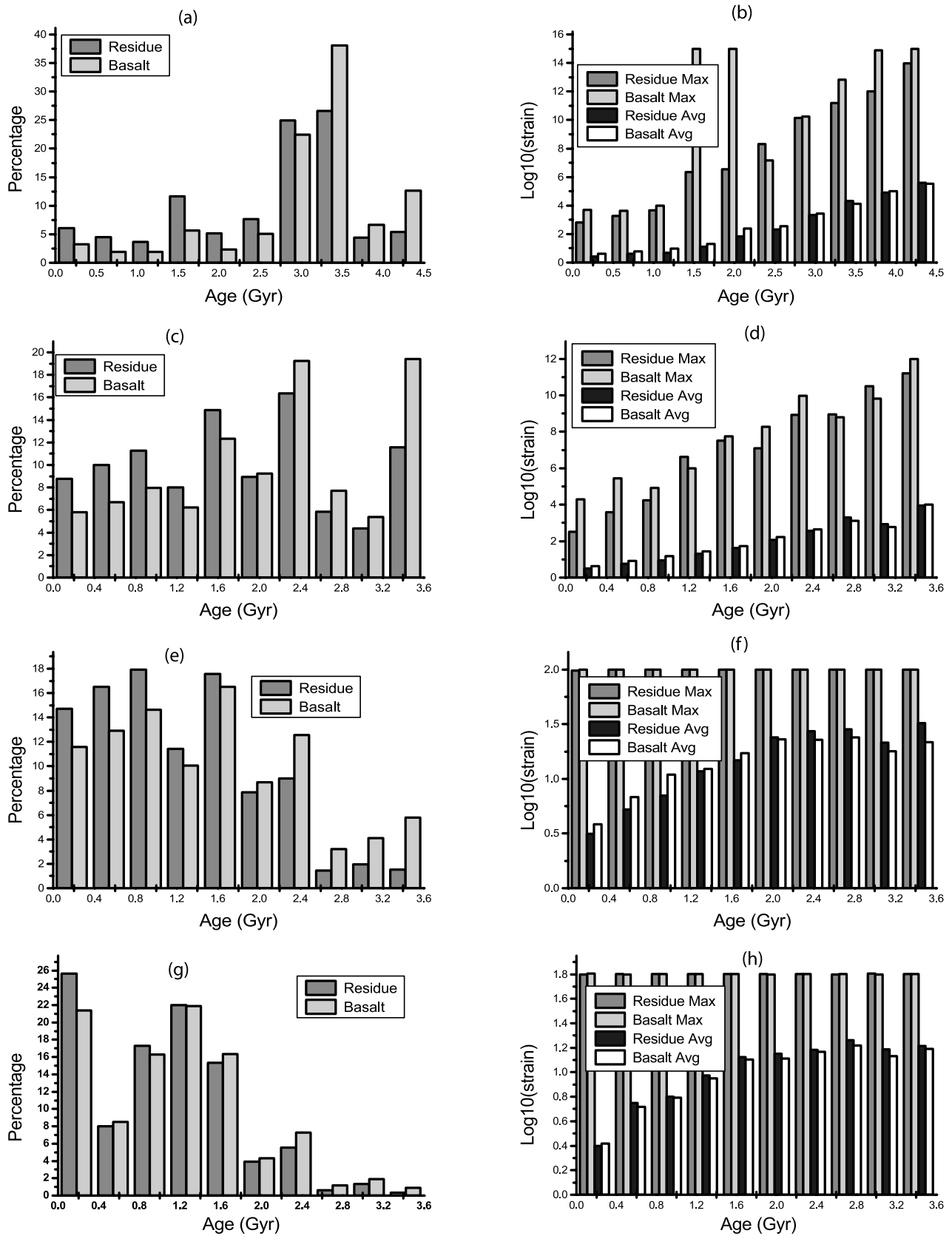


Figure 10. (left) Age distribution of tracers and (right) dependence of strain on age. “Average” denotes the geometric mean. (a) and (b) The 4.5 Gyr run, (c) and (d) 3.6 Gyr run, (e) and (f) as Figures 10c and 10d but not including tracers with strain $>10^2$, and (g) and (h) 3.6 Gyr case with strain resetting during the run, threshold 60.

[75] These plots show that the main effect of increased sampling region is to reduce scatter, with minimal effect on the slope and associated isotopic age: around 2.5 Gyr in these cases. Thus sampling volume cannot offer an explanation for the discrepancy between isotopic slopes in the model and in Earth.

3.4.5. Effect of Crustal Density

[76] *Christensen and Hofmann* [1994] found that the obtained Pb-Pb age depends on the density of crustal material in the deep mantle: with increasing density, it resides longer in the deep layer; thus the slope and its age increase. In order to test the effect of this in the present model, the three different crustal density profiles shown in Figure 3 are tried, in the context of a 3.6 Gyr run with strain threshold of 60, which gives a realistic slope. As shown in Figures 8j, 8k, and 8l, a similar trend is obtained with the current model. In the case with dense crust the obtained $^{206}\text{Pb}/^{204}\text{Pb}$ ratio (Figure 8j) is between 17.0 and 21.0, and the $^{207}\text{Pb}/^{204}\text{Pb}$ ratio is between 15.2 and 15.8, which are the ranges found for MORB and HIMU (Figure 1). The average isotope ratios of erupted magmas in the final part of the run (indicated by the arrow lines) lie within the observed range of MORB values. The slope is about 0.122, which gives an age of 1.99 Gyr. It is curious that two trends are visible on the diagram. This seems to suggest that early differentiation is slowly destroyed by later mantle mixing and the strain resetting processes. The obtained $^{147}\text{Sm}/^{144}\text{Nd}$ ratio (Figure 8f) is between 0.12 and 0.25, and the $^{143}\text{Nd}/^{144}\text{Nd}$ ratio is between 0.5127 ($\epsilon_{\text{Nd}} = 1.2$) and 0.5134 ($\epsilon_{\text{Nd}} = 14.8$), which is the range found for MORB and HIMU (Figure 2). The age determined by the Sm-Nd system is 1.3 Gyr, which is lower than the Pb age. The case with neutrally buoyant crust at the CMB (Figure 8k) has a slightly smaller slope (0.12) and age (1.96 Gyr), while the case with buoyant crust at the CMB has an even smaller slope (Figure 8l), corresponding to an age of 1.79 Gyr.

[77] Thus the results display the same trend as those of *Christensen and Hofmann* [1994]. However, the range of age variation with deep mantle crustal density is only 0.2 Gyr, from about 2.0 to 1.8 Gyr, which is small compared to other effects discussed in sections 3.4.1–3.4.4.

3.4.6. Discretization Noise

[78] Statistical noise in Pb ratios caused by the discretization of composition into individual tracers can amplify old heterogeneities that are actually mixed, thereby increasing the apparent age. *Christensen and Hofmann* [1994] found this to be unimportant except in a case with no chemical buoyancy, in which correcting for it decreased the Pb-Pb age by 32%. This analysis has been performed on the present cases, i.e., making “random data” by random assignment of tracers to sampling cells, followed by subtraction of the random data covariance matrix from the “real data” covariance matrix. For most cases this results in a small correction hence does not affect the conclusions of this study. In particular, for the 4.5 Gyr case with no added effects (Figure 8a) the slope is reduced from 0.28 to 0.21, reducing the isotopic age from 3.39 to 2.91 Gyr, still much too large. With HIMU production only in the last 2.5 Gyr (Figure 8b) the age is corrected from 1.75 Gyr to 1.71 Gyr. With a strain threshold and local isotope redistribution (Figure 8c) the age is corrected from 3.18 to 2.96 Gyr. This analysis is strictly correct only for Gaussian data so needs to

be tested in future by simply increasing the number of tracers.

4. Conclusions and Discussion

4.1. Summary of Findings

[79] The model mantle develops significant stratification in its major element composition, including a deep layer of subducted crust above the CMB that does not have a sharp top like layers that are inserted a priori [e.g., *Montague et al.*, 1998]; this gradual boundary makes it more difficult for plumes to form. A local stratification also builds up either side of the 660 km discontinuity, with crustal-enriched material in the transition zone and depleted material at the top of the lower mantle. This local stratification is due to the two-component phase transitions around 660–720 km depth [*Fleitout et al.*, 2000; *Ogawa*, 2000; *Tackley*, 2002a].

[80] Heat flux and convective vigor (velocity) decrease with time, but differently (e.g., less strongly) from what is commonly assumed in parameterized evolution models. In the early history, magmatism carries a large fraction of the surface heat flow, with conductive heat flow remaining approximately constant over time. These scalings must be systematically determined in future modeling efforts.

[81] The slope in the $^{207}\text{Pb}/^{204}\text{Pb}$ – $^{206}\text{Pb}/^{204}\text{Pb}$ diagram for a 4.5 Gyr evolution is very much larger than observed, corresponding to an effective age of 3.4 Gyr, or 2.9 Gyr after a noise correction. This is due to the signature being dominated by material that melted early in the modeled evolution, when melting was much more vigorous. Five possible shortcomings of the model that might account for this discrepancy were explored:

[82] 1. The size of the sampling region (over which isotopic ratios are calculated) has minimal effect on the slope, merely decreasing the scatter of the synthetic data.

[83] 2. The density of subducted crust in the deep mantle affects how long it resides in a layer above the CMB. It is found to have a small effect on calculated age (consistent with [*Christensen and Hofmann*, 1994]), but it can only account for about 0.2 Gyr of variation, insufficient to explain the discrepancy.

[84] 3. If HIMU material does not enter the mantle prior to 2.0–2.5 Gyr before present [*Martin*, 1986; *Elliott et al.*, 1999], our model produces isotopic ages in the range of 1.4–1.75 Gyr, suggesting that it may account for the discrepancy.

[85] 4. More frequent remelting of crustal material can also erase the signature of older heterogeneities, greatly reducing the age, but this requires that the melting rate was substantially higher in the past and that the fraction of mantle carrying the radiogenic isotopic signature is small.

[86] 5. Erasure of heterogeneities by stretching, which has been proposed to be the major way in which isotopic heterogeneities are erased [e.g., *Christensen*, 1989; *Kellogg and Turcotte*, 1990], was investigated and found to decrease the age, although is insufficient to explain the discrepancy by itself.

[87] Which of these is most important? Stretching 5 is certainly operating and should be taken into account, but is insufficient to explain the observed isotopic ages by itself, so it is necessary to appeal additionally to either non-production of HIMU in the first ~half of Earth history,

and/or greater melting in the past. In the main previous numerical modeling effort of Pb-Pb ages [Christensen and Hofmann, 1994], realistic slopes were obtained by a combination of shorter (3.6 Gyr) model time, more frequent remelting, and constant convective vigor.

4.2. Other Model Shortcomings

[88] It is useful to consider other possible shortcomings of the model and how they might affect the results:

[89] 1. The convective vigor is lower than Earth-like, with an RMS surface velocity that fluctuates around 1.0 cm yr^{-1} . Despite this, the total amount of melting that takes place over model history is within plausible bounds, as discussed in section 3.4.2. This indicates that in partial compensation for lower surface velocity, higher degrees of melting and thus a thicker oceanic crust have been formed, which reduces the concentration of incompatible trace elements in the crust. While this should not affect isotope ratios for highly incompatible species, it affects absolute concentrations and thus, for example, findings about how much heat-producing elements can be stored in a basal layer [Coltice and Ricard, 1999]. Lower convective vigor also reduces strain rates, so that stretching occurs less rapidly than it would in the real Earth. Thus absolute stretching amounts calculated here are not directly applicable to Earth.

[90] 2. Continents are not present in the model. Other than the various dynamical and heat flow effects that continents have [e.g., Zhong and Gurnis, 1993; Lenardic, 1998; Lowman and Jarvis, 1999; Grigne and Labrosse, 2001], the continental crust and lithosphere are thought to be important geochemically, acting as a storage place for trace elements. The continuous and ongoing extraction of the continental crust changes mantle average composition with time, and the return of parts of it into the mantle are thought to be responsible for some of the geochemically observed end-members, namely, EM1 and EM2 [Hofmann, 1997]. For example, Kellogg *et al.* [2002] successfully modeled the development of Sm-Nd and Rb-Sr signatures considering only the continent-mantle system with no oceanic cycle present. In general, continuous extraction of continental material with higher Pb/U than the mantle would be expected to decrease the mantle Pb-Pb isochron.

[91] 3. The presented calculations are in two dimensions. This likely affects the rate and character of stirring compared to three-dimensional geometry, although the overall sign of the effect is not clear: When the flow is purely poloidal, mixing is slower in three dimensions than in two dimensions [Schmalzl *et al.*, 1995, 1996], but the presence of toroidal flow can greatly increase stirring [Ferrachat and Ricard, 1998; Van Keken and Zhong, 1999]. Two dimensionality also prevents the existence of columnar plumes, which would allow a distinction to be made between MORB and plume-related basalts.

4.3. Outlook

[92] Numerical thermochemical convection models with tracking of trace elements are a promising approach for studying Earth evolution, and several further developments are possible in future. Modeling results need to be further analyzed and understood, which could be done by relating them to parameterized models in terms of residence times and fluxes [e.g., Coltice *et al.*, 2000] as well as by

developing a better understanding of the scaling of melting rate, velocity etc. with convective parameters. Future models could also be made more realistic, particularly by introducing continents, which should allow the full range of geochemical end-members to develop, allowing investigation of more complex issues such as the “kappa conundrum” [Elliott *et al.*, 1999].

[93] Because chemical heterogeneity likely exists at all length scales down to centimeters, it will not be possible in the foreseeable future to resolve all of the relevant length scales, particularly in three dimensions, so extrapolation and parameterization will continue to be necessary to treat the smallest length scales. However, various features of this extrapolation could be further studied, such as the size spectrum of heterogeneities, and the parameterization could be more sophisticated than the present treatment, a useful first step being the statistical approach of Kellogg *et al.* [2002]. Use of increasingly higher resolutions will also allow the extrapolations to be better investigated and tested.

[94] The details of heterogeneity in the source region are particularly interesting in the light of recent suggestions for the origin of MORB-OIB differences, which have traditionally been attributed to different source regions [Hofmann, 1997], with a more sophisticated mechanism for maintaining different source regions recently being proposed [Albarède and van der Hilst, 2002]. Meibom *et al.* [2002, 2003] and Meibom and Anderson [2004], however, argue that actually MORB and OIB isotope ratios come from the same distribution, with OIBs simply exhibiting greater scatter. Detailed isotopic evolution modeling [Kellogg, 2004; Kellogg *et al.*, 2002] indicates that the source region may contain a “plum pudding” of the opposite sense to previously proposed [Allègre and Turcotte, 1986], with plums of depleted material amidst a relatively enriched matrix consisting of various short-length-scale components: OIBs sample the matrix, whereas MORBs sample both. Other intriguing possibilities have also been proposed, such as two-stage melting [Morgan and Morgan, 1999], or a transition zone water filtering [Bercovici and Karato, 2003].

[95] **Acknowledgments.** This research was supported by Los Alamos National Laboratory, the David and Lucile Packard Foundation, NSF grant EAR0207741, and NASA grant NAG 5-3956. Reviews by R. W. Carlson, F. Albarède, and one anonymous reviewer were very helpful in improving this manuscript.

References

- Albarède, F. (2001), Radiogenic ingrowth in systems with multiple reservoirs: Applications to the differentiation of the mantle-crust system, *Earth Planet. Sci. Lett.*, *189*, 59–73.
- Albarède, F., and R. D. van der Hilst (2002), Zoned mantle convection, *Philos. Trans. R. Soc. London, Ser. A*, *360*(1800), 2569–2592.
- Allègre, C. J., and E. Lewin (1995), Isotopic systems and stirring times of the Earth's mantle, *Earth Planet. Sci. Lett.*, *136*, 629–646.
- Allègre, C. J., and D. L. Turcotte (1986), Implications of a two-component marble-cake mantle, *Nature*, *323*, 123–127.
- Allègre, C. J., O. Brèvert, B. Duprè, and J. F. Minster (1980), Isotopic and chemical effects produced in a continuously differentiating convecting Earth mantle, *Philos. Trans. R. Soc. London, Ser. A*, *297*, 447–477.
- Armstrong, R. L., and S. M. Hein (1973), Computer simulation of Pb and Sr isotope evolution of the Earth's crust and upper mantle, *Geochim. Cosmochim. Acta*, *37*, 1–18.
- Barth, M. G., R. L. Rudnick, I. Horn, W. F. McDonough, M. J. Spicuzza, J. W. Valley, and S. E. Haggerty (2001), Geochemistry of xenolithic eclogites from west Africa, part I: A link between low MgO eclogites and Archean crust formation, *Geochem. Cosmochim. Acta*, *65*, 1499–1527.

- Bercovici, D., and S. Karato (2003), Whole-mantle convection and the transition-zone water filter, *Nature*, **425**, 39–44.
- Blichert-Toft, J., and F. Albarède (1994), Short-lived chemical heterogeneities in the Archean mantle with implications for mantle convection, *Science*, **263**, 1593–1596.
- Carlson, R. W. (1987), Geochemical evolution of the crust and mantle, *Rev. Geophys.*, **25**(5), 1011–1020.
- Carlson, R. W. (1994), Mechanisms of Earth differentiation - consequences for the chemical structure of the mantle, *Rev. Geophys.*, **32**(4), 337–361.
- Chase, C. G. (1981), Oceanic island Pb: Two-stage histories and mantle evolution, *Earth Planet. Sci. Lett.*, **52**, 277–284.
- Chase, C. G., and P. J. Patchett (1988), Stored mafic/ultramafic crust and early Archean mantle depletion, *Earth Planet. Sci. Lett.*, **91**, 66–72.
- Chauvel, C., S. L. Goldstein, and A. W. Hofmann (1995), Hydration and dehydration of oceanic crust controls Pb evolution in the mantle, *Chem. Geol.*, **126**, 65–75.
- Christensen, U. R. (1989), Mixing by time-dependent convection, *Earth Planet. Sci. Lett.*, **95**(3–4), 382–394.
- Christensen, U. R., and A. W. Hofmann (1994), Segregation of subducted oceanic crust in the convecting mantle, *J. Geophys. Res.*, **99**(B10), 19,867–19,884.
- Christensen, U. R., and D. A. Yuen (1985), Layered convection induced by phase transitions, *J. Geophys. Res.*, **90**(B12), 10,291–10,300.
- Coltice, N., and Y. Ricard (1999), Geochemical observations and one layer mantle convection, *Earth Planet. Sci. Lett.*, **174**, 125–137.
- Coltice, N., S. Ferrachat, and Y. Ricard (2000), Box modeling the chemical evolution of geophysical systems: Case study of the Earth's mantle, *Geophys. Res. Lett.*, **27**, 1579–1582.
- Conrad, C. P., and B. H. Hager (1999), The thermal evolution of an Earth with strong subduction zones, *Geophys. Res. Lett.*, **26**, 3041–3044.
- Davies, G. F. (2002), Stirring geochemistry in mantle convection models with stiff plates and slabs, *Geochim. Cosmochim. Acta*, **66**, 3125–3142.
- Doe, B. R., and R. E. Zartman (1979), Plumbotectonics I, the Phanerozoic, in *Geochemistry of Hydrothermal Ore Deposits*, edited by H. L. Barnes, pp. 22–70, John Wiley, New York.
- Dupré, B., and C. J. Allègre (1983), Pb-Sr isotope variation in Indian Ocean basalts and mixing phenomena, *Nature*, **303**, 142–146.
- du Vignaux, N. M., and L. Fleitout (2001), Stretching and mixing of viscous blobs in Earth's mantle, *J. Geophys. Res.*, **106**(B12), 30,893–30,908.
- Elliott, T., A. Zindler, and B. Bourdon (1999), Exploring the kappa conundrum: The role of recycling in the lead isotope evolution of the mantle, *Earth Planet. Sci. Lett.*, **169**, 129–145.
- Ferrachat, S., and Y. Ricard (1998), Regular vs. chaotic mantle mixing, *Earth Planet. Sci. Lett.*, **155**, 75–86.
- Ferrachat, S., and Y. Ricard (2001), Mixing properties in the Earth's mantle: Effects of the viscosity stratification and of oceanic crust segregation, *Geochem. Geophys. Geosyst.*, **2**, doi:10.1029/2000GC000092.
- Fleitout, L., A. Mambole, and U. Christensen (2000), Phase changes around 670 km depth and segregation in the Earth's mantle, *Eos Trans. AGU*, **81**(41), Fall Meet. Suppl., Abstract T12E-11.
- Grigne, C., and S. Labrosse (2001), Effects of continents on earth cooling: Thermal blanketing and depletion in radioactive elements, *Geophys. Res. Lett.*, **28**, 2707–2710.
- Gurnis, M., and G. Davies (1986a), The effect of depth-dependent viscosity on convective mixing in the mantle and the possible survival of primitive mantle, *Geophys. Res. Lett.*, **13**, 541–544.
- Gurnis, M., and G. Davies (1986b), Mixing in numerical models of mantle convection incorporating plate kinematics, *J. Geophys. Res.*, **91**, 6375–6395.
- Hart, S. R. (1984), A large-scale isotope anomaly in the Southern Hemisphere mantle, *Nature*, **309**, 753–757.
- Herzberg, C., P. Raterron, and J. Zhang (2000), New experimental observations on the anhydrous solidus for peridotite KLB-1, *Geochem. Geophys. Geosyst.*, **1**, doi:10.1029/2000GC000089.
- Hoffman, N. R. A., and D. P. McKenzie (1985), The destruction of geochemical heterogeneities by differential fluid during mantle convection, *Geophys. J. R. Astron. Soc.*, **82**, 163–206.
- Hofmann, A. W. (1988), Chemical differentiation of the Earth: The relationship between mantle, continental crust, and oceanic crust, *Earth Planet. Sci. Lett.*, **90**, 297–314.
- Hofmann, A. W. (1997), Mantle geochemistry: The message from oceanic volcanism, *Nature*, **385**, 219–229.
- Hofmann, A. W., and W. M. White (1982), Mantle plumes from ancient oceanic crust, *Earth Planet. Sci. Lett.*, **57**, 421–436.
- Holland, H. D. (1984), *The Chemical Evolution of the Atmosphere and Oceans*, 582 pp., Princeton Univ. Press, Princeton, N. J.
- Holland, H. D. (1994), Early Proterozoic atmospheric change, in *Early Life on Earth*, edited by S. Bengtson, pp. 237–244, Columbia Univ. Press, New York.
- Jochum, K., et al. (1983), K, U and Th in mid-ocean ridge basalt glasses and heat production, K/U and K/Rb in the mantle, *Nature*, **306**, 431–436.
- Kellogg, J. B. (2004), Towards an understanding of chemical and isotopic heterogeneity in the Earth's mantle, Ph.D. thesis, Harvard Univ., Cambridge, Mass.
- Kellogg, J. B., S. B. Jacobsen, and R. J. O'Connell (2002), Modeling the distribution of isotopic ratios in geochemical reservoirs, *Earth Planet. Sci. Lett.*, **204**, 182–202.
- Kellogg, L. H., and D. L. Turcotte (1990), Mixing and the distribution of heterogeneities in a chaotically convecting mantle, *J. Geophys. Res.*, **95**, 421–432.
- Klein, E. M., C. H. Langmuir, A. Zindler, H. Staudigel, and B. Hamelin (1988), Isotope evidence of a mantle convection boundary at the Australian-Antarctic Discordance, *Nature*, **333**, 623–629.
- Korenaga, J. (2003), Energetics of mantle convection and the fate of fossil heat, *Geophys. Res. Lett.*, **30**(8), 1437, doi:10.1029/2003GL016982.
- Lenardic, A. (1998), On the partitioning of mantle heat loss below oceans and continents over time and its relationship to the Archean paradox, *Geophys. J. Int.*, **134**, 706–720.
- Lithgow-Bertelloni, C., M. A. Richards, Y. Ricard, R. J. O'Connell, and D. C. Engebretson (1993), Toroidal-poloidal partitioning of plate motions since 120 Ma, *Geophys. Res. Lett.*, **20**, 375–378.
- Lowman, J. P., and G. T. Jarvis (1999), Effects of mantle heat source distribution on supercontinent stability, *J. Geophys. Res.*, **104**, 12,733–12,746.
- Martin, H. (1986), Effect of steeper archaic geothermal gradient on geochemistry of subduction zone magmas, *Geology*, **14**, 753–756.
- Masters, G., G. Laske, H. Bolton, and A. M. Dziewonski (2000), The relative behavior of shear velocity, bulk sound speed, and compressional velocity in the mantle: Implications for chemical and thermal structure, in *Earth's Deep Interior: Mineral Physics and Tomography From the Atomic to the Global Scale*, *Geophys. Monogr. Ser.*, vol. 117, edited by S. I. Karato et al., pp. 63–87, AGU, Washington, D. C.
- McKenzie, D. (1979), Finite deformation during fluid flow, *Geophys. J. R. Astron. Soc.*, **58**, 689–715.
- Meibom, A., and D. L. Anderson (2004), The statistical upper mantle assemblage, *Earth Planet. Sci. Lett.*, **217**, 123–139.
- Meibom, A., N. H. Sleep, C. P. Chamberlain, R. G. Coleman, R. Frei, M. T. Hren, and J. L. Wooden (2002), Re-Os isotopic evidence for long-lived heterogeneity and equilibration processes in the Earth's upper mantle, *Nature*, **419**, 705–708.
- Meibom, A., D. L. Anderson, N. H. Sleep, R. Frei, C. P. Chamberlain, M. T. Hren, and J. L. Wooden (2003), Are high He-3/He-4 ratios in oceanic basalts an indicator of deep-mantle plume components?, *Earth Planet. Sci. Lett.*, **208**, 197–204.
- Michard, A., and F. Albarède (1985), Hydrothermal uranium uptake at ridge crests, *Nature*, **317**, 61–88.
- Montague, N. L., L. H. Kellogg, and M. Manga (1998), High Rayleigh number thermo-chemical models of a dense boundary layer in D'' , *Geophys. Res. Lett.*, **25**, 2345–2348.
- Moresi, L. N., and V. S. Solomatov (1995), Numerical investigation of 2D convection with extremely large viscosity variations, *Phys. Fluids*, **7**, 2154–2162.
- Moresi, L. N., and V. Solomatov (1998), Mantle convection with a brittle lithosphere—Thoughts on the global tectonic styles of the Earth and Venus, *Geophys. J. Int.*, **133**, 669–682.
- Morgan, J. P., and W. J. Morgan (1999), Two-stage melting and the geochemical evolution of the mantle: A recipe for mantle plum-pudding, *Earth Planet. Sci. Lett.*, **170**, 215–239.
- Murakami, M., K. Hirose, K. Kawamura, N. Sata, and Y. Ohishi (2004), Post-perovskite phase transition in MgSiO_3 , *Science*, **304**, 855–858.
- Nakagawa, T., and P. J. Tackley (2004), Effects of thermo-chemical mantle convection on the thermal evolution of the Earth's core, *Earth Planet. Sci. Lett.*, **220**, 107–119.
- Newsom, H. E., W. M. White, K. P. Jochum, and A. W. Hofmann (1986), Siderophile and chalcophile element abundances in oceanic basalts, *Earth Planet. Sci. Lett.*, **80**, 299–313.
- Oganov, A. R., and S. Ono (2004), Theoretical and experimental evidence for a post-perovskite phase of MgSiO_3 in Earth's D'' layer, *Nature*, **430**, 445–448.
- OGAWA, M. (2000), Coupled magmatism-mantle convection system with variable viscosity, *Tectonophysics*, **322**, 1–18.
- Olson, P., D. Yuen, and D. Balsiger (1984), Mixing of passive heterogeneities by mantle convection, *J. Geophys. Res.*, **89**, 425–436.
- Ono, S., E. Ito, and T. Katsura (2001), Mineralogy of subducted basaltic crust (MORB) from 25 to 37 GPa, and chemical heterogeneity of the lower mantle, *Earth Planet. Sci. Lett.*, **190**, 57–63.
- Pearson, D. G., G. R. Davies, and P. H. Nixon (1993), Geochemical constraints on the petrogenesis of diamond facies pyroxenites from the Beni Bousera peridotite massif, north Morocco, *J. Petrol.*, **34**, 125–172.

- Reisberg, I., and A. Zindler (1986), Extreme isotopic variability in the upper mantle: Evidence from Ronda, *Earth Planet. Sci. Lett.*, *81*, 29–45.
- Ringwood, A. E. (1990), Slab-mantle interactions: 3. Petrogenesis of intraplate magmas and structure of the upper mantle, *Chem. Geol.*, *82*, 187–207.
- Saal, A. E., S. R. Hart, N. Shimizu, E. H. Hauri, and G. D. Layne (1998), Pb isotopic variability in melt inclusions from oceanic island basalts, Polynesia, *Science*, *282*, 1481–1484.
- Schilling, J. G. (1973), Iceland mantle plume: Geochemical study of Reykjanes ridge, *Nature*, *242*, 565–571.
- Schmalzl, J., G. A. Houseman, and U. Hansen (1995), Mixing properties of three-dimensional stationary convection, *Phys. Fluids*, *21*, 1027–1033.
- Schmalzl, J., G. A. Houseman, and U. Hansen (1996), Mixing in vigorous, time-dependent three-dimensional convection and application to the Earth's mantle, *J. Geophys. Res.*, *101*, 21,847–21,858.
- Scott, D. R., and D. J. Stevenson (1989), A self-consistent model of melting, magma migration and buoyancy-driven circulation beneath mid-ocean ridges, *J. Geophys. Res.*, *94*, 2973–2988.
- Silver, P. G., R. W. Carlson, and P. Olson (1988), Deep slabs, geochemical heterogeneity, and the large-scale structure of mantle convection: Investigation of an enduring paradox, *Annu. Rev. Earth Planet. Sci.*, *16*, 477–541.
- Solomatov, V. S., and L. N. Moresi (1996), Stagnant lid convection on Venus, *J. Geophys. Res.*, *101*, 4737–4753.
- Stacey, F. D. (1992), *Physics of the Earth*, 3rd ed., 513 pp., Brookfield, Kenmore, Australia.
- Steinbach, V., and D. Yuen (1994), Effects of depth-dependent properties on the thermal anomalies produced in flush instabilities from phase transitions, *Phys. Earth Planet. Inter.*, *86*, 165–183.
- Suen, C. J., and F. A. Frey (1987), Origins of the mafic and ultramafic rocks in the Ronda peridotite, *Earth Planet. Sci. Lett.*, *85*, 183–202.
- Tackley, P. J. (1996a), Effects of strongly variable viscosity on three-dimensional convection in planetary mantles, *J. Geophys. Res.*, *101*, 3311–3332.
- Tackley, P. J. (1996b), On the ability of phase transitions and viscosity layering to induce long wavelength heterogeneity in the mantle, *Geophys. Res. Lett.*, *23*, 1985–1988.
- Tackley, P. J. (1998), Three-dimensional simulations of mantle convection with a thermo-chemical basal boundary layer: D'' ?, in *The Core-Mantle Boundary Region*, *Geodyn. Ser.*, vol. 28, edited by M. Gurnis et al., pp. 231–253, AGU, Washington, D. C.
- Tackley, P. J. (2000a), Self-consistent generation of tectonic plates in time-dependent, three-dimensional mantle convection simulations: 1. Pseudoplastic yielding, *Geochem. Geophys. Geosyst.*, *1*, doi:10.1029/2000GC000036.
- Tackley, P. J. (2000b), Self-consistent generation of tectonic plates in time-dependent, three-dimensional mantle convection simulations: 2. Strain weakening and asthenosphere, *Geochem. Geophys. Geosyst.*, *1*, doi:10.1029/2000GC000043.
- Tackley, P. (2002a), Avalanches revisited: Does the pyroxene-garnet system aid or abet phase change-induced mantle layering?, *Eos Trans. AGU*, *83*(47), Fall Meet. Suppl., Abstract MR72B-1043.
- Tackley, P. J. (2002b), Strong heterogeneity caused by deep mantle layering, *Geochem. Geophys. Geosyst.*, *3*(4), 1024, doi:10.1029/2001GC000167.
- Tackley, P. J., and S. D. King (2003), Testing the tracer ratio method for modeling active compositional fields in mantle convection simulations, *Geochem. Geophys. Geosyst.*, *4*(4), 8302, doi:10.1029/2001GC000214.
- Tackley, P. J., and D. J. Stevenson (1993), A mechanism for spontaneous self-perpetuating volcanism on the terrestrial planets, in *Flow and Creep in the Solar System: Observations, Modeling and Theory*, edited by D. B. Stone and S. K. Runcorn, pp. 307–322, Kluwer Acad., Norwell, Mass.
- Tackley, P. J., and S. Xie (2002), The thermochemical structure and evolution of Earth's mantle: Constraints and numerical models, *Philos. Trans. R. Soc. London, Ser. A*, *360*, 2593–2609.
- Tackley, P. J., and S. Xie (2003), STAG3D: A code for modeling thermochemical multiphase convection in Earth's mantle, in *Second MIT Conference on Computational Fluid and Solid Mechanics*, edited by K. J. Bathe, pp. 1524–1527, Elsevier Sci., New York.
- Tackley, P. J., D. J. Stevenson, G. A. Glatzmaier, and G. Schubert (1994), Effects of multiple phase transitions in a three-dimensional spherical model of convection in Earth's mantle, *J. Geophys. Res.*, *99*, 15,877–15,901.
- van Der Hilst, R. D., S. Widlyantoro, and E. R. Engdahl (1997), Evidence for deep mantle circulation from global tomography, *Nature*, *386*, 78–84.
- Van Keken, P. E. (2001), Cylindrical scaling for dynamical cooling models of the Earth, *Phys. Earth Planet. Inter.*, *124*, 119–130.
- Van Keken, P. E., and C. J. Ballentine (1998), Whole-mantle versus layered mantle convection and the role of a high-viscosity lower mantle in terrestrial volatile evolution, *Earth Planet. Sci. Lett.*, *156*, 19–32.
- Van Keken, P. E., and C. J. Ballentine (1999), Dynamical models of mantle volatile evolution and the role of phase transitions and temperature-dependent rheology, *J. Geophys. Res.*, *104*, 7137–7151.
- Van Keken, P. E., and S. Zhong (1999), Mixing in a 3D spherical model of present day mantle, *Earth Planet. Sci. Lett.*, *171*, 533–547.
- White, W. M. (1993), $^{238}\text{U}/^{204}\text{Pb}$ in MORB and open system evolution of the depleted mantle, *Earth Planet. Sci. Lett.*, *115*, 211–226.
- Xie, S., and P. J. Tackley (2004), Evolution of helium and argon isotopes in a convecting mantle, *Phys. Earth Planet. Inter.*, *146*, 417–439.
- Zerr, A., A. Diegeler, and R. Boehler (1998), Solidus of Earth's deep mantle, *Science*, *281*, 243–246.
- Zhong, S., and M. Gurnis (1993), Dynamic feedback between a continent-like raft and thermal convection, *J. Geophys. Res.*, *98*, 12,219–12,232.
- Zindler, A., and S. Hart (1986), Chemical geodynamics, *Earth Planet. Sci. Lett.*, *14*, 493–571.

P. J. Tackley and S. Xie, Department of Earth and Space Sciences, University of California, Los Angeles, CA 90095, USA. (ptackley@ess.ucla.edu; sxie@ess.ucla.edu)